

HST Observations of X-ray-selected AGN

David Schade¹, B.J.Boyle², & Michael Letawsky¹

¹ *Dominion Astrophysical Observatory, 5071 West Saanich Road, Victoria, V8X 4M6, Canada*

² *Anglo-Australian Observatory, PO Box 296, Epping, NSW 1710, Australia*

ABSTRACT

We report on the initial results of a comprehensive Hubble Space Telescope (HST) snapshot imaging survey of 76 low redshift ($z < 0.15$) X-ray-selected active galactic nuclei (AGN) in the Einstein Extended Medium Sensitivity Survey. This survey is expected to show no bias with respect to host galaxy types and so is arguably one of the best available samples with HST imaging for the study of the host galaxies. The HST observations in the F814W band are complemented by deeper ground-based observations in the B and R bands for all AGN. The absolute magnitudes for AGN in this sample lie in the range $-24 < M_{B(\text{AB})} < -18$, bracketing the extrapolated break in the QSO luminosity function ($M_{B(\text{AB})} = -22.3$) at these low redshifts. We find a weak correlation between the luminosity of the host galaxy and the central AGN. We find no convincing cases of an AGN with no detectable host galaxy, although the faintest host galaxies of moderately luminous AGN do extend as faint as $M_{B(\text{AB})} = -18$. We find no evidence for strong interaction/merger activity in any of the AGN in this sample. The median ratio of AGN to host galaxy luminosity ($L_{\text{AGN}}/L_{\text{Host}} = 0.2$) is lower than previously observed, although the observed scatter is large. Approximately 55 per cent of these radio-quiet AGN have host galaxies that are fit best by a ‘bulge-only’ model (or alternatively are classified visually as ellipticals/S0 galaxies) confirming the result by McLure et al. that radio-quiet AGN are not exclusively found in spiral galaxies. A comparison with the Autofib field galaxy survey shows that the morphological type distribution is skewed toward earlier types than a field galaxy sample drawn at random with the same distribution of luminosities. This is consistent with the observation that the luminosity of the host galaxies is higher by 0.75 ± 0.25 mag than a matching sample drawn from the Autofib survey. Given the bias toward early-type galaxies, the AGN host galaxies are consistent with a luminosity and size distribution identical to normal galaxies. In every respect these galaxies are intermediate in their properties between the large, luminous host galaxies found around high luminosity AGN in the local Universe and the fainter host galaxies identified around lower luminosity Seyfert galaxies. These results suggest that, with the exception of a bias toward early spectral types, host galaxies of AGN are drawn at random from the overall galaxy population with the nuclear properties governed (weakly) by spheroid mass.

Key words: X-rays: general – galaxies: active – quasars: general

1 INTRODUCTION

The properties of the host galaxies of active galactic nuclei (AGN) and QSOs play a fundamental role in our understanding of the AGN phenomenon. The size, luminosity and structure of the host galaxy can provide valuable clues to the origin and fuelling of AGN (e.g. Smith & Heckman 1990). Ground-based optical imaging studies of low redshift AGN over the past 20 years (see e.g. Adams 1977, Simkin, Su and Schwarz 1980, Smith et al. 1986, MacKenty 1990, Zitelli et al. 1993, Kontilainen & Ward 1994) have been limited by the spatial resolution attainable from the ground; $1 \text{ arcsec} \equiv 2.8 h_{50}^{-1} \text{ kpc}$ at $z = 0.1$, and no strong consensus

has been reached over the general properties of AGN host galaxies from such studies (see e.g. Vèron-Cetty and Woltjer 1990).

More recently, near infra-red imaging studies of AGN have yielded a clearer picture (McLeod & Reike 1994, Dunlop et al. 1993, Taylor et al. 1996). Infra-red studies, of course, not only benefit from the improved seeing in the H and K bands, but also because of the increased dominance of the red host galaxy against the blue AGN. Such studies reveal that powerful AGN inhabit luminous ($L > L^*$) and massive ($r_{1/2} > 10 \text{ kpc}$) galaxies. Furthermore, these studies find that radio-loud AGN are found exclusively in early-type galaxies. Taylor et al. (1996) also found early-

type galaxies acting as hosts for almost half of the radio-quiet AGN in their sample, challenging the existing orthodoxy that radio-quiet AGN are predominantly found in spiral galaxies.

With the excellent imaging performance provided by the COSTAR-corrected optics, a number of QSO host galaxy studies have recently been carried out with the HST (Bachall et al. 1997, Boyce et al. 1997, McLure et al. 1999). These studies each contain typically 15–20 QSOs and confirm many of the earlier results obtained in the infra-red. The predominantly bright ($M_B < -23$) QSOs imaged by the HST appear to lie in bright ($L > L^*$) with large radii ($r_{1/2} > 10$ kpc). McLure et al. (1999) also confirm their previous finding that a significant fraction (90 per cent) of the radio-quiet QSOs imaged have elliptical hosts.

An extremely comprehensive HST imaging study of 256 AGN and starbursts has also been carried out by Malkan, Gorjian & Tam (1998). This study has focussed on much lower redshift ($z < 0.035$) and consequently lower luminosity AGN. This survey also confirms the tendency for a significant fraction of broad-line radio-quiet AGN to reside in earlier type galaxies. In contrast to studies of bright AGN, few of the AGN host galaxies in this study show direct evidence for interactions or recent merger activity.

Despite careful selection of the object sample, all these studies have relied heavily on existing heterogeneous compilations of QSO catalogues (see e.g. Vèron and Vèron-Cetty 1997) on which to base their initial target list. In particular they have focussed on luminous optically-selected or radio-selected QSOs, where strong selection effects may favour particular, and possibly non-representative types of QSOs. For example, the Palomar-Green (PG) survey (Green, Schmidt & Liebert 1986) is the source of many of QSOs used in the studies above, yet it is strongly biased toward star-like images in the original photographically-identified sample.

Imaging surveys of radio-selected AGN also avoid the problem associated with optical selection biases, but such objects only comprise ~ 5 per cent of all AGN (Peacock, Miller & Mead 1986) and so inferences drawn from such samples are limited to a small fraction of the AGN population.

With limitations for both optically-selected and radio-selected AGN samples, the increasing availability of complete, X-ray-selected samples of AGN offers an alternative method to study of AGN host galaxies. Unlike radio samples, X-ray AGN do form a representative sample of all AGN; there being few, if any, X-ray-quiet AGN (Avni & Tanenbaum 1986). In addition, X-ray flux limited samples with *complete* optical identification suffer from none of the inherent biases towards dominant nuclei or peculiar morphological types present in existing optically-selected samples of low redshift AGN.

X-ray-selected samples of AGN have been studied in the past; Kontilainen & Ward (1994) carried out ground-based optical and near-infra-red imaging of 31 AGN in the 2 – 10 keV sample of Piccinotti et al. (1982), and Malkan, Margon & Chanan (1984) obtained optical images for 24 AGN selected from the 0.3 – 3.5 keV Einstein Medium Sensitivity Survey (EMSS, Stocke et al. 1991). The AGN studied by Kontilainen & Ward (1994) were heavily weighted towards extremely low redshifts ($z < 0.015$) and thus were

of low luminosity ($M_B > -21$). Conversely, the Malkan et al. survey comprised a wide range of much higher redshift objects ($0.1 < z < 1.8$), although the ground-based imaging gave inconclusive results for the nine AGN with $z > 0.4$ and limited results on the properties of the host galaxy associated with the lower redshift AGN.

Nevertheless, the EMSS is an extremely powerful sample of AGN to use. With near-complete optical identification (94 per cent), it does not suffer from any strong optical biases. Over 95 per cent of the sample is radio-quiet, including all of the AGN with $z < 0.2$. For $z < 0.15$ the spatial resolution of the HST is ideally suited to the study of the innermost regions ($< 400h_{50}^{-1}$ pc) of the host galaxy.

We therefore initiated an imaging campaign with HST to obtain snapshot F814W observations of approximately 100 AGN in the EMSS with $0.03 < z < 0.15$. The magnitude range spanned by these AGN is $-24 < M_{B(AB)} < -18$, straddling the predicted ‘break’ luminosity ($M_{B(AB)} \sim -22.3$) in the AGN luminosity function (LF) at these redshifts (Boyle et al. 1988).

An important aspect to this programme is that we also have ground-based imaging in the B and R passbands from the 1-m Jacobus Kapteyn Telescope (JKT) and 40-inch telescope operated by the Mount Stromlo and Siding Spring Observatories (MSSSO) to complement the HST observations. Although the ground-based images were only taken in moderate seeing conditions (1 arcsec – 3 arcsec) they are complementary to the HST data, permitting us to model the host galaxy accurately well beyond the central regions, to surface brightness levels ($B_\mu = 26$ mag arcsec $^{-2}$) unattainable with the snapshot HST observations.

In this paper we report on the results obtained from the 76 AGN imaged in this programme. We describe the HST and ground-based observations in section 2. In section 3 we discuss the fitting procedure used, including the technique of 2-dimensional profile fitting used to extract information on the AGN host galaxy. We present our results in section 4, comparing the properties of AGN host galaxies derived from this study with those obtained from previous observations. We summarise our conclusions in section 5.

2 DATA

2.1 The AGN sample

The AGN sample used in this imaging study were selected from the EMSS (Stocke et al. 1991). Over 830 X-ray sources were identified in the EMSS, of which 420 were classified as AGN, i.e., as having broad emission lines. The EMSS was selected in the ‘soft’ X-ray band 0.3 – 3.5 keV, with a mean flux limit of $S(0.3 - 3.5 \text{ keV}) \sim 10^{-13} \text{ erg s}^{-1} \text{ cm}^{-2}$.

We selected 80 low redshift ($z < 0.15$) AGN for our imaging study. Our imaging campaign began with observations made at the 1-m JKT and so our sample was initially defined to be those low redshift EMSS AGN that were observable from La Palma. However, the subsequent success of our HST snapshot proposal led us to expand the sample to include a further 13 EMSS QSOs at southern declinations. Follow-up ground-based observations for these QSOs was

carried out on the MSSSO 40-inch telescope. The ground-based studies and the HST imaging campaigns were largely carried out in parallel over the period 1993 – 1998. The unpredictability of both the weather in the ground-based observations and the sequence of images obtained in snapshot mode meant that it was impossible to maintain an exact correspondence between the AGN imaged in the ground-based and HST programs.

We obtained a total of 76 snapshot images with the HST. These AGN form the basis of the sample analysed in this paper. We have some form of ground-based B or R imaging data for 69 of these AGN; of these 11 have only B -band imaging and 2 have R -band imaging only. Positions, redshifts and observational details for all AGN are listed in Table 1. Positions and redshifts were taken from the revised EMSS catalogue published by Maccacaro et al. (1995).

Fig. 1 illustrates the region of the AGN absolute magnitude-redshift plane sampled by this study. In this diagram we have plotted the catalogued redshift against total (nuclear + host) $M_{B(AB)}$ magnitudes for each AGN in the sample. The magnitudes were derived from the HST and ground-based images using the fitting procedures described below. The AGN span a range $-23.6 < M_{B(AB)} < -18.5$, with a median luminosity $M_{B(AB)} < -21.5$.

All magnitudes given in the present paper are in the AB system. For the ground-based observations, we adopted the following transformations from the Landolt system: $B_{AB} = B - 0.17$ and $R_{AB} = R + 0.05$. Throughout this paper we use $H_0 = 50h_{50} \text{ km s}^{-1} \text{ Mpc}^{-1}$, $\Omega_M = 1$, $\Omega_\Lambda = 0$.

Eight of the EMSS AGN in our data set were classified by Stocke et al. (1991) as uncertain or ambiguous AGN, usually because the identification spectra lack sufficient signal-to-noise to determine the presence of broad Balmer emission lines. More detailed spectroscopy of ‘ambiguous’ EMSS AGN by Boyle et al. (1995) has shown that these sources are a mix of AGN (Seyfert 1.5 – 2) and star-forming galaxies. The only ambiguous AGN in this data set that was also studied by Boyle et al. (1995) is MS1334.6+0351 which was classified by Boyle et al. (1995) as a Seyfert 1.5 on the basis of its broad $H\alpha$ emission line. For this analysis, MS1334.6+0351 was therefore classified as a bona fide AGN, whereas the remainder of these objects were treated as uncertain AGN.

2.2 HST observations

HST WFPC2 observations were obtained for all 76 AGN listed in Table 1 as part of a Cycle 6 snapshot program. The observations used in this analysis were obtained over the period May 1996 to January 1999; the date of each snapshot observation is given in Table 1. The observations were carried out in the F814W (I) passband, chosen to assist in the detection of the redder host galaxy components over the bluer nucleus. Each snapshot observation lasted for 600 sec, comprising three separate 200-sec exposures. In each case, the AGN was imaged at the centre of the Planetary Camera (PC), with a pixel scale of $0.0455 \text{ arcsec pixel}^{-1}$ thus maximising the resolution attainable. For a few of the brightest objects in the sample, a short (10 sec) exposure was also taken to obtain an unsaturated image of the nuclear component. Fig. 2 shows the central $30 \text{ arcsec} \times 30 \text{ arcsec}$ region of the reduced HST image for each AGN in the sample.

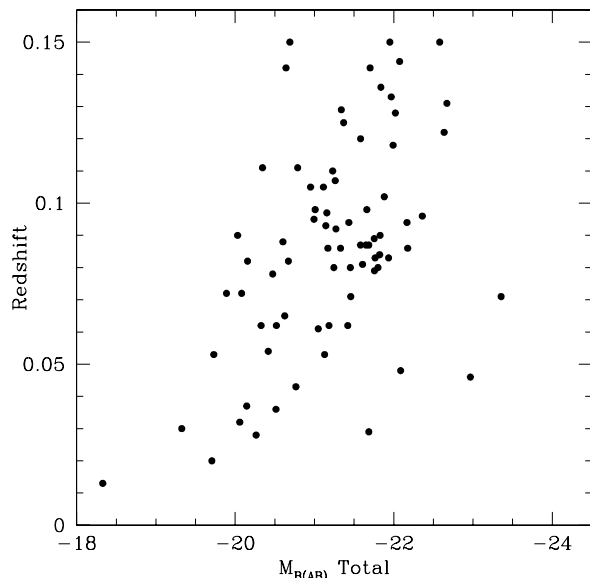


Figure 1. Absolute Magnitude $v.$ redshift for the 76 AGN in this sample.

The data were processed using standard STSDAS pipelines including flat-fielding and bias-subtraction. The three images of each object were obtained using an integer-shift dithering pattern. The images were combined using these offsets and taking the median of the images which resulted in the removal of warm pixels and cosmic rays. Photometric zeropoints were obtained using the header information and converting to the AB system $m_{AB} = -2.5 \log f_\nu + 48.6$. Saturation was dealt with by replacing saturated pixels with re-scaled unsaturated pixels from the 10-sec integrations where available. Otherwise saturated pixels were defined as unusable and were ignored in the fitting process.

2.3 Ground-based imaging

Ground-based observations in the B and R passbands were carried out on the 1-m JKT and the 40-inch MSSSO telescope. Harris B and R filter sets were used on both telescopes. The JKT observations were made over three observing seasons: 1993 January 18–24, 1994 January 4–10 and 1995 January 4–10. The observations in 1993 and 1994 were made with a 700×500 -pixel GEC chip ($0.35 \text{ arcsec pixel}^{-1}$) and the 1995 observations were made with a 1024^2 -pixel Tektronix chip ($0.31 \text{ arcsec pixel}^{-1}$). An equivalent of nine nights’ data were obtained over the three runs, with the 1994 run providing the best conditions. B -band observations were carried out exclusively in 1993 and 1994, with R -band observations made in 1995.

Additional imaging for the southern QSOs in our target list was obtained with the MSSSO 40-inch telescope equipped with a 1024^2 Tektronix CCD ($0.25 \text{ arcsec pixel}^{-1}$) on the nights of 1997 July 28–31. Only 1.5 nights’ data in poor seeing ($> 2 \text{ arcsec}$) were obtained.

Table 1 gives the total integration time and median seeing of the images for each AGN, together with the telescope used to obtain the ground-based images. Observations of each AGN were split into a number of short exposures,

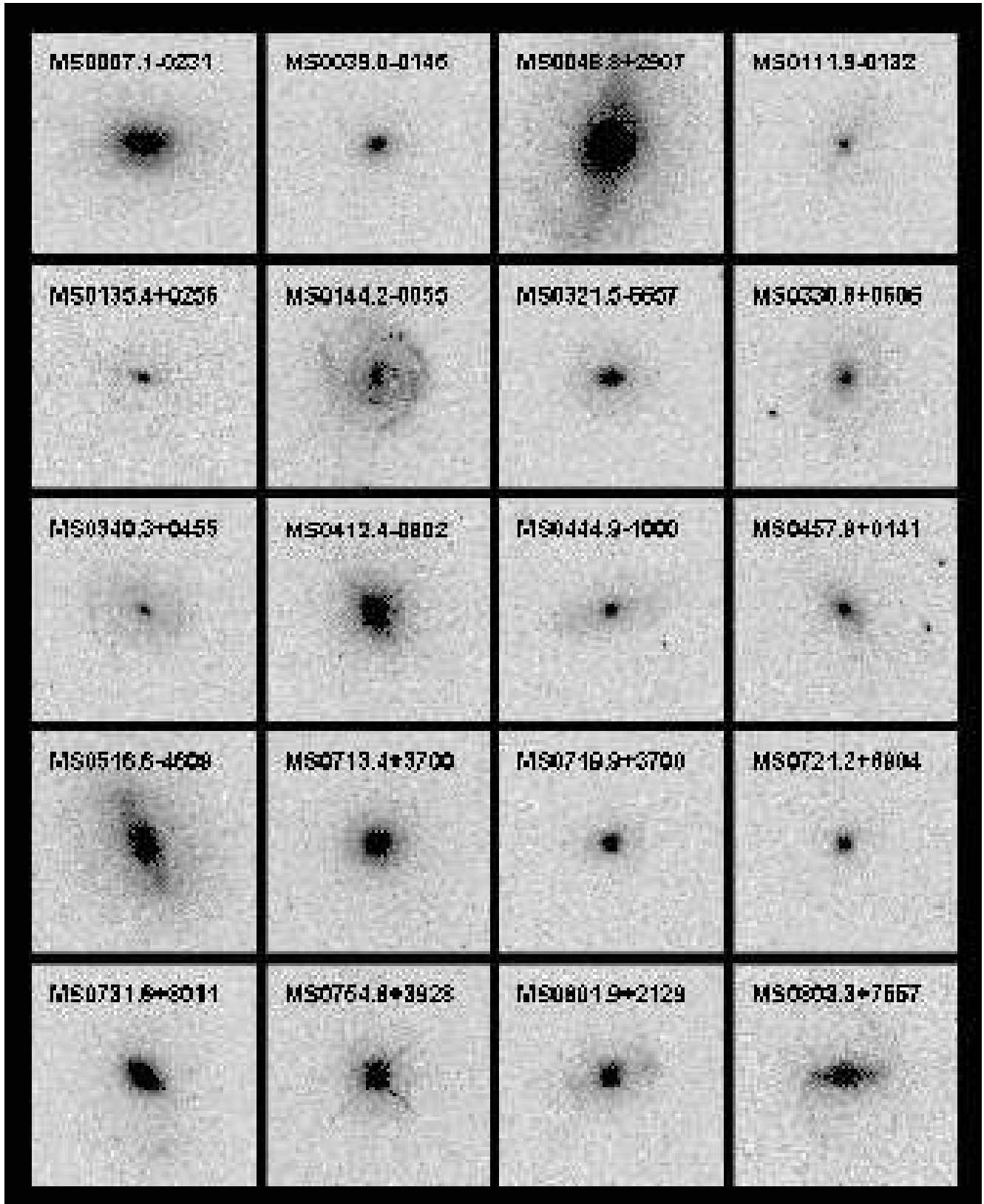


Figure 2 Reduced HST snapshot image for each EMSS AGN in the survey. Each image is 30 arcsec \times 30 arcsec

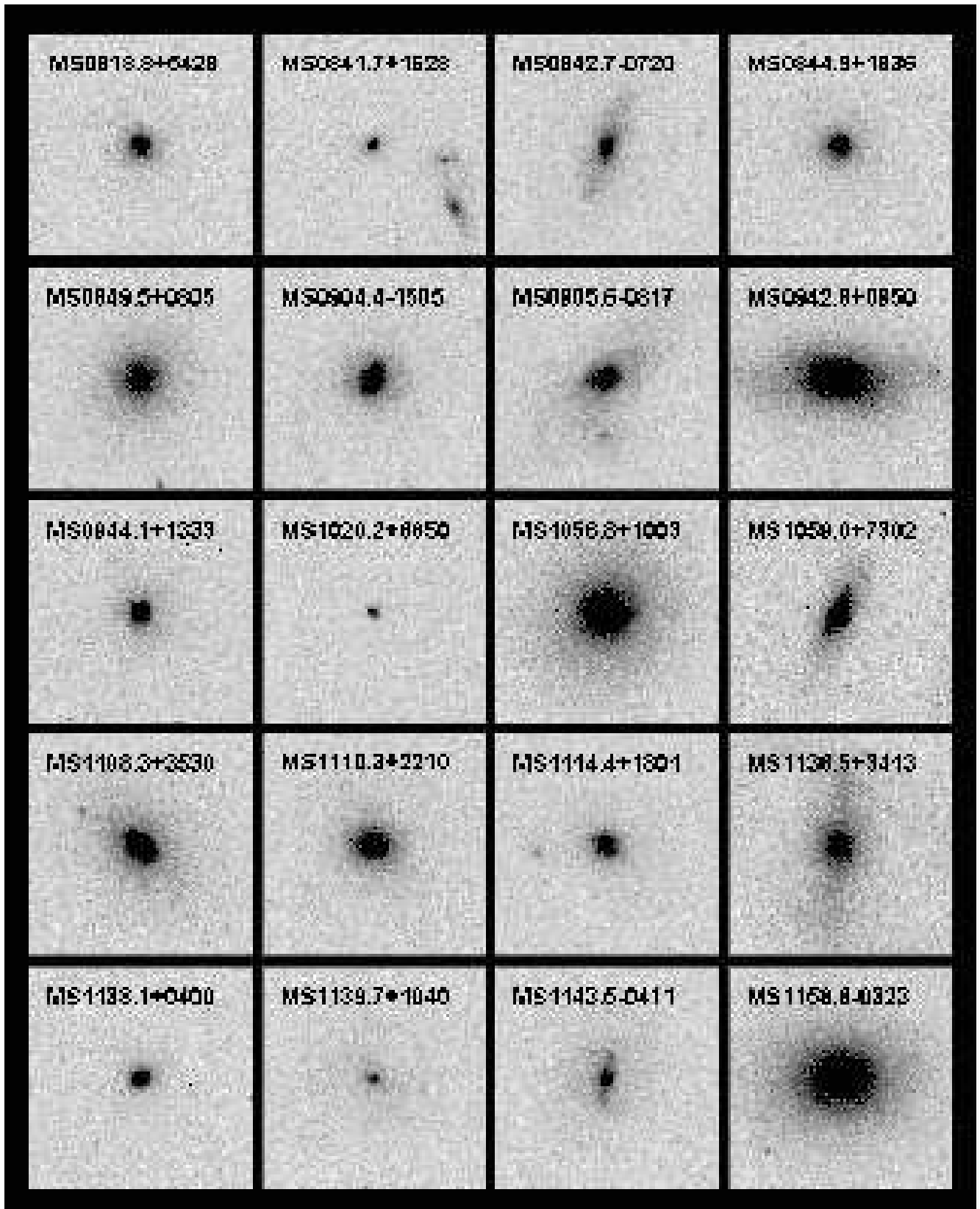


Figure 2 contd.

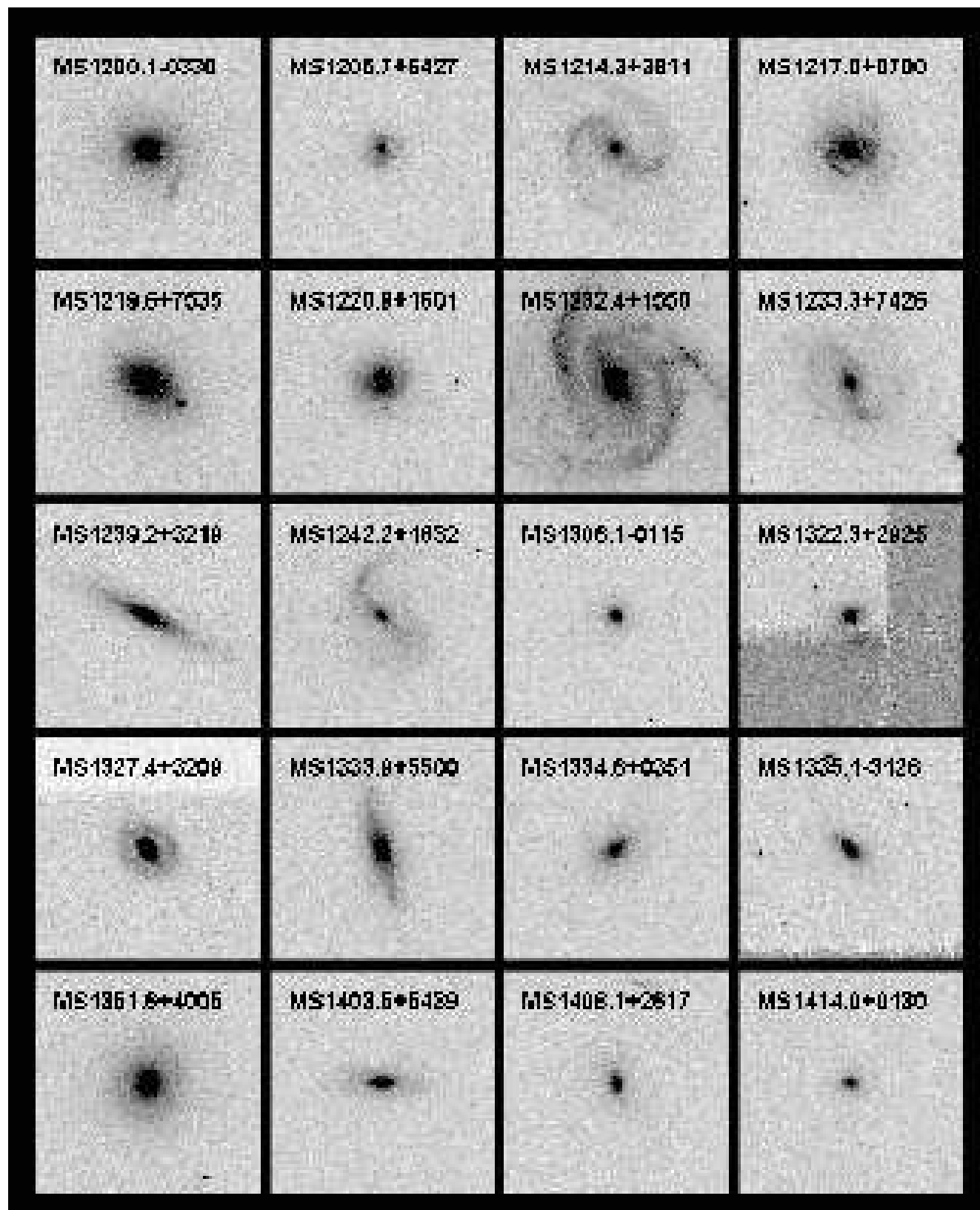


Figure 2 contd.

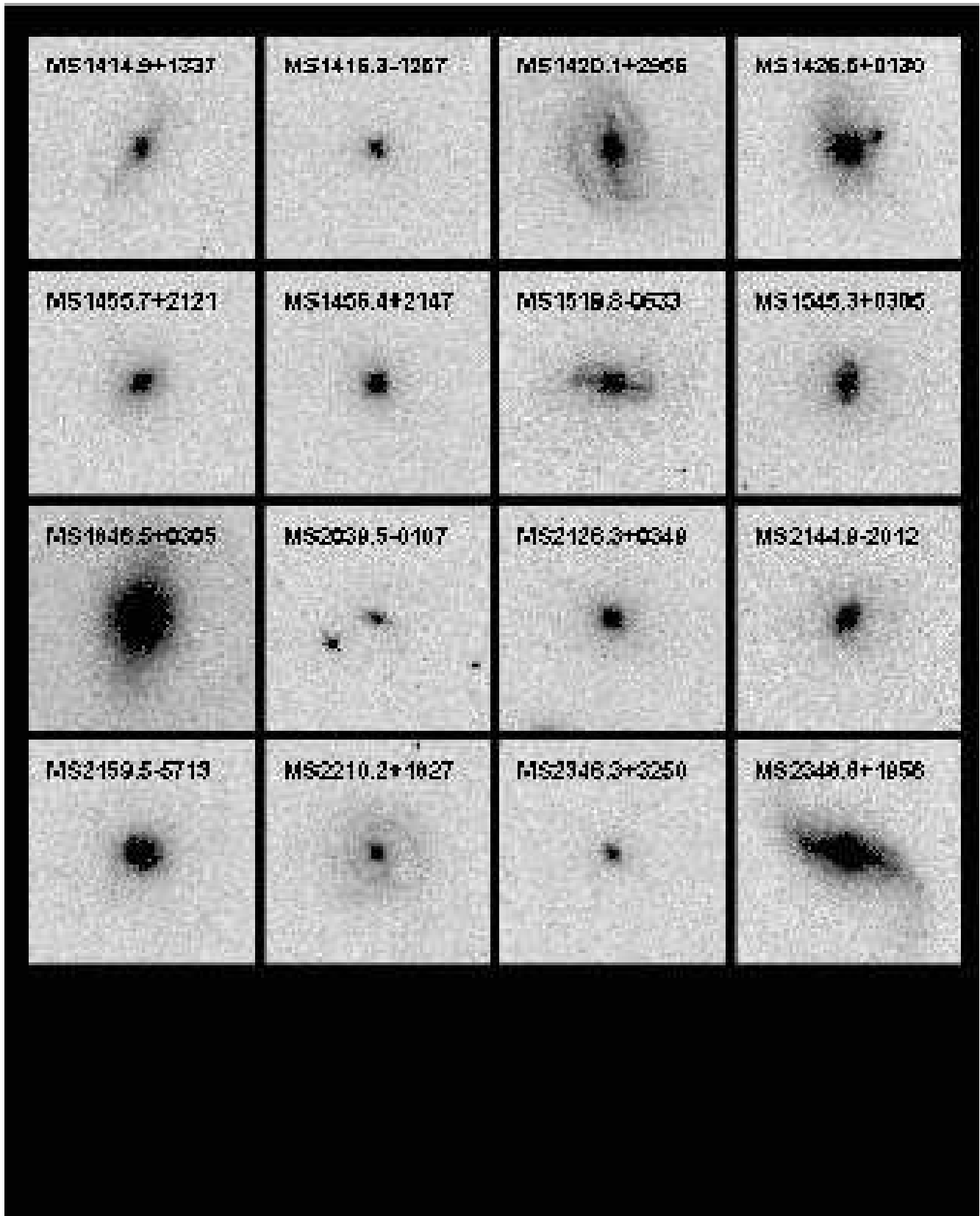


Figure 2 contd.

Table 1. AGN observed in the imaging survey

Name	z	RA (1950) Dec						Telescope	<i>B</i>		Telescope	<i>R</i>		Date of HST obs
		h	m	s	°	'	"		Exposure (secs)	FWHM (arcsecs)		Exposure (secs)	FWHM (arcsecs)	
MS0007.1–0231	0.087	0	7	5.8	–2	31	18	MSSSO	4800	2.9	MSSSO	1200	4.3	10/1/97
MS0039.0–0145†	0.11	0	39	03.4	–1	45	40	—	—	—	—	—	—	20/7/96
MS0048.8+2907	0.036	0	48	53.1	29	7	55	JKT	3600	2.7	JKT	900	2.3	29/9/96
MS0111.9–0132	0.120	1	11	54.2	–1	32	25	JKT	4800	1.3	—	—	—	19/01/99
MS0135.4+0256	0.150	1	35	29.2	2	55	36	JKT	3600	1.9	JKT	900	2.7	14/11/96
MS0144.2–0055	0.080	1	44	11.3	–0	55	41	—	—	—	—	—	—	20/7/96
MS0321.5–6657	0.093	3	21	41.0	–66	57	44	MSSSO	2400	2.6	—	—	—	26/3/97
MS0330.8+0606	0.105	3	30	52.9	6	6	38	JKT	4800	1.6	JKT	900	1.3	19/7/96
MS0340.3+0455†	0.097	3	40	16.8	4	55	38	—	—	—	—	—	—	16/3/97
MS0412.4–0802	0.037	4	12	27.3	–8	3	8	JKT	3600	2.8	JKT	1200	3.0	12/7/96
MS0444.9–1000†	0.095	4	44	53.6	–10	0	51	JKT	3600	1.2	JKT	900	2.8	17/4/97
MS0457.9+0141	0.128	4	57	56.8	1	41	49	JKT	3600	1.3	JKT	900	1.7	13/4/97
MS0516.6–4609	0.048	5	16	37.7	–46	09	19	—	—	—	—	—	—	25/4/97
MS0713.4+3700	0.122	7	13	29.5	36	59	58	JKT	3600	1.2	JKT	900	1.7	18/3/97
MS0719.9+7100	0.125	7	19	58.2	71	0	14	JKT	3600	1.8	JKT	1800	2.3	31/5/96
MS0721.2+6904	0.111	7	21	14.5	69	3	49	JKT	3600	1.5	JKT	900	2.7	5/6/96
MS0731.6+8011	0.087	7	31	45.4	80	10	44	—	—	—	—	—	—	13/7/96
MS0754.6+3928	0.096	7	54	38.7	39	28	36	JKT	2050	1.2	JKT	900	1.8	3/4/97
MS0801.9+2129	0.118	8	1	56.6	21	29	24	JKT	8400	1.5	JKT	2700	2.4	21/10/96
MS0803.3+7557	0.094	8	3	20.1	75	57	39	JKT	7200	1.7	JKT	900	2.9	24/3/97
MS0818.8+5428	0.086	8	18	46.8	54	28	14	JKT	3600	1.8	JKT	1800	3.0	21/3/97
MS0841.7+1628	0.150	8	41	40.4	16	27	49	JKT	3600	1.1	JKT	1800	2.1	7/4/97
MS0842.7–0720	0.144	8	42	43.1	–7	21	8	JKT	3600	1.7	JKT	900	2.8	17/4/97
MS0844.9+1836	0.086	8	44	57.9	18	35	44	JKT	6000	1.1	JKT	900	2.1	12/4/97
MS0849.5+0805	0.063	8	49	34.6	8	4	56	—	—	—	JKT	900	2.3	26/4/97
MS0904.4–1505	0.054	9	4	26.6	–15	5	38	JKT	2400	1.9	JKT	900	2.7	19/4/97
MS0905.6–0817	0.071	9	5	38.4	–8	17	39	JKT	3600	1.6	JKT	900	2.2	12/4/97
MS0942.8+0950†	0.013	9	42	49.3	9	50	0	JKT	1200	1.8	JKT	900	2.2	19/10/96
MS0944.1+1333	0.131	9	44	10.1	13	33	47	JKT	3600	0.9	JKT	900	2.0	31/3/97
MS1020.2+6850	0.078	10	20	19.1	68	50	10	JKT	2750	2.1	JKT	900	2.8	24/3/97
MS1058.8+1003†	0.028	10	58	49.8	10	3	27	JKT	3600	1.7	JKT	900	2.4	26/3/97
MS1059.0+7302	0.089	10	59	7.7	73	2	47	JKT	3600	3.1	JKT	900	2.9	14/9/96
MS1108.3+3530	0.061	11	8	20.8	35	30	8	JKT	3600	1.8	JKT	900	2.6	2/4/97
MS1110.3+2210†	0.030	11	10	19.0	22	10	52	JKT	3600	2.2	JKT	900	2.3	8/4/97
MS1114.4+1801†	0.092	11	14	25.8	18	1	3	JKT	4800	1.3	JKT	900	1.8	7/4/97
MS1136.5+3413	0.032	11	36	36.0	34	12	27	JKT	3600	1.8	JKT	900	2.0	25/3/97
MS1138.1+0400	0.098	11	38	7.3	4	0	44	JKT	3600	1.1	JKT	900	1.8	3/12/96
MS1139.7+1040	0.150	11	39	42.0	10	40	16	JKT	3600	1.4	JKT	900	1.8	2/2/97
MS1143.5–0411	0.133	11	43	30.5	–4	11	21	—	—	—	—	—	—	21/12/96
MS1158.6–0323	0.020	11	58	40.6	–3	23	58	JKT	3600	3.4	JKT	1200	3.1	30/3/97
MS1200.1–0330	0.065	12	0	11.5	–3	30	40	JKT	3600	2.9	JKT	900	1.9	30/12/96
MS1205.7+6427	0.105	12	5	45.1	64	27	27	JKT	3600	1.5	JKT	900	2.3	25/3/97
MS1214.3+3811	0.062	12	14	21.8	38	11	16	JKT	2400	2.1	JKT	900	2.1	21/10/96
MS1217.0+0700	0.080	12	16	58.0	7	0	12	JKT	2400	1.1	JKT	900	1.9	11/4/97
MS1219.6+7535	0.070	12	19	33.8	75	35	16	JKT	3600	1.9	JKT	900	2.3	10/3/97
MS1220.9+1601	0.081	12	20	59.0	16	1	43	JKT	3600	1.5	JKT	900	1.8	12/4/97
MS1232.4+1550	0.046	12	32	25.0	15	50	26	JKT	3600	1.7	JKT	900	2.1	8/4/97
MS1233.3+7426	0.084	12	33	18.4	74	26	37	JKT	4800	2.1	JKT	900	2.2	8/12/98
MS1239.2+3219	0.053	12	39	19.5	32	19	21	JKT	3600	1.8	JKT	900	2.2	28/10/96
MS1242.2+1632	0.087	12	42	11.6	16	32	33	JKT	2400	1.1	JKT	900	2.5	29/3/97
MS1306.1–0115	0.111	13	6	11.4	–1	14	55	JKT	4800	1.0	JKT	900	2.3	8/4/97
MS1322.3+2925	0.072	13	22	19.8	29	25	51	JKT	2400	1.7	—	—	—	16/8/96
MS1327.4+3209	0.093	13	27	27.8	32	9	8	JKT	4800	1.8	JKT	900	2.0	8/5/97
MS1333.9+5500	0.107	13	33	56.6	55	0	5	JKT	3600	1.3	JKT	900	1.7	16/10/96
MS1334.6+0351†	0.136	13	34	37.8	3	51	11	MSSSO	2400	2.5	MSSSO	2400	3.2	7/4/97

†Uncertain/ambiguous ID from Stocke et al. (1991)

Table 1 contd.

Name	z	RA (1950) Dec						Telescope	B		Telescope	R		Date of HST obs
		h	m	s	°	'	"		Exposure (secs)	FWHM (arcsecs)		Exposure (secs)	FWHM (arcsecs)	
MS1335.1–3128	0.082	13	35	10.3	–31	28	42	MSSSO	2400	2.8	MSSSO	1200	3.5	28/8/96
MS1351.6+4005	0.062	13	51	38.8	40	5	44	JKT	2400	1.8	—	—	—	4/7/96
MS1403.5+5439	0.082	14	3	30.4	54	39	15	JKT	2700	1.3	JKT	900	2.0	17/3/97
MS1408.1+2617	0.072	14	8	8.8	26	17	35	JKT	4800	1.1	JKT	900	1.8	24/8/96
MS1414.0+0130	0.142	14	14	07.1	1	30	18	MSSSO	2400	3.1	—	—	—	29/3/97
MS1414.9+1337	0.088	14	14	58.0	13	37	18	JKT	3600	1.5	JKT	900	1.9	2/9/96
MS1416.3–1257	0.129	14	16	21.3	–12	56	58	MSSSO	2700	4.3	—	—	—	7/4/97
MS1420.1+2956	0.053	14	20	8.7	29	56	30	JKT	2400	1.9	JKT	900	3.5	16/3/97
MS1426.5+0130	0.086	14	26	33.9	1	30	27	—	—	—	—	—	—	29/3/97
MS1455.7+2121	0.080	14	55	44.4	21	21	53	JKT	3600	1.6	JKT	900	2.0	19/3/97
MS1456.4+2147	0.062	14	56	27.6	21	48	5	JKT	3600	1.9	—	—	—	29/3/97
MS1519.8–0633	0.083	15	19	49.0	–6	34	1	MSSSO	4800	3.7	MSSSO	1200	3.5	11/3/97
MS1545.3+0305	0.098	15	45	21.2	3	5	1	MSSSO	2400	3.1	—	—	—	5/9/96
MS1846.5–7857	0.029	18	46	33.4	–78	57	33	MSSSO	1200	3.7	MSSSO	1800	4.4	24/4/97
MS2039.5–0107	0.142	20	39	30.8	–01	08	06	MSSSO	2400	2.5	—	—	—	29/3/97
MS2128.3+0349	0.094	21	28	21.8	3	49	18	MSSSO	2400	2.8	—	—	—	4/4/97
MS2144.9–2019	0.102	21	44	57.3	–20	12	08	MSSSO	9600	2.7	—	—	—	21/7/96
MS2159.5–1050	0.083	21	59	30.3	–57	14	09	—	—	—	—	—	—	11/3/97
MS2210.2+1827	0.079	22	10	13.6	18	27	34	JKT	2200	2.2	JKT	900	2.3	30/12/96
MS2348.3+3250†	0.090	23	48	21.4	32	51	08	—	—	—	JKT	900	2.5	17/5/97
MS2348.6+1956	0.045	23	48	41.3	19	57	2	JKT	3600	2.2	JKT	2700	2.7	27/1/97

†Uncertain/ambiguous ID from Stocke et al. (1991)

‡Uncertain/ambiguous ID from Stocke et al. (1991), confirmed as AGN by Boyle et al. (1995)

typically 1200 sec for B -band observations and 900 sec for R -band observations.

As far as possible during the observing runs, we attempted to match the prevailing seeing conditions with the redshift of the AGN currently being observed, thus preserving, as far as possible, a constant physical size for the resolution. Observations of some AGN were repeated until a lower FWHM (< 2 arcsec) was achieved. Since the ground-based images were primarily used to provide information on the larger angular scales (e.g. bulge and particularly disk) where the HST images provide less information, good seeing was not considered as important as image depth. Some images with very poor seeing still provided useful constraints at large angular scales on the fitting process, improving the overall 3-component fit.

We reduced the CCD frames using the IRAF package at the Cambridge STARLINK node and at the DAO. Standard techniques were used to bias-correct and flat-field the data. We created flat-fields for each night by averaging sky-limited data frames from different AGN fields, after bright stars had been masked out and other deviant points rejected using a 3 σ clipping algorithm.

Based on 3–4 Landolt (1992) standard star sequences we observed each night, we were able to obtain a zeropoint consistent to ± 2 per cent on each night on which observations were carried out.

2.4 HST and ground-based imaging

A feature of this analysis is the complementary information provided by the ground- and space-based images. The ground-based observations provide low-resolution data that

is suitable for defining the extended disk component (even with poor seeing) while the HST observations provide the information on small spatial scales required to deconvolve the strongly peaked ($r^{1/4}$) galaxy bulge and point source contributions. The relative levels of signal-to-noise are such that the HST data are only moderately effective at characterising the host galaxy properties (because of their 600-sec integration times) on large scales. The low-resolution ground-based imaging provides effective constraints at large radii but has little power to discriminate between bulge and point-source components.

The choice of filters reinforces the role of each dataset. We chose the F814W imaging from HST to emphasize the redder bulge component relative to the bluer nuclear source. By the same token, the bluer B and R filters in the ground-based observations provide important colour information on the outer regions of the galaxy.

3 PROFILE FITTING

3.1 Method

To derive the observed parameters for the different AGN components, we performed a simultaneous three-component parametric model fit to the B , R and I images for each AGN in the sample. The components fitted were a point source, an exponential disk, and a de Vaucouleurs $r^{1/4}$ bulge. In this procedure the specified model was transformed into the observational space of each dataset using the pixel scale, detector orientation, filter, and point spread function (PSF) appropriate for each image.

For the ground-based images, the PSF was derived from several (typically five) bright stars in the same image that contained the AGN. The PSFs were defined and managed using the DAOPHOT package (Stetson 1987) within IRAF. The core of ground-based observations was fitted with a gaussian function and the residuals were retained as a lookup table.

For the HST images, the PSF was fitted using a Lorentzian function plus a look-up table of residuals. Sampling errors are severe with HST and simulations showed that these can be substantially reduced in our fitting procedure by using DAOPHOT to construct the PSF for each observation centered at the same position (with respect to the pixel grid) as the observed object before the fitting procedure begins.

Very few of the HST observations had suitable PSF stars on the PC chip. Therefore, a single PSF constructed from several bright stars in a star cluster observations was used to fit all of the galaxies. We were able to check the adopted PSF against seven stellar PSFs observed in this sample, where a PSF star was present near the AGN. After processing the stellar PSFs in the same manner as done for the fitting procedure, the FWHM for the PSFs showed a full range of 0.11 PC pixels (0.005 arcsec). As a result the normalisation of the PSF is not exact, leading to a photometric errors at 2 – 3 per cent level when measured with a 0.05 arcsec aperture.

Details of the fitting procedure are described by Schade et al. (1996). The bulge component is characterised by:

$$I_B(r_B) = I_B(0) \exp \left[-7.67 \left(\frac{r_B}{r_e} \right)^{0.25} \right]$$

and the disk component by:

$$I_D(r_D) = I_D(0) \exp \left(-\frac{r_D}{h} \right)$$

where $I(0)$ is the central surface brightness, r_e is the bulge effective (or half-light) radius, and h is the disk scale length. The point source is simply a scaled version of the PSF and is assumed to be coincident with the galaxy center (we found no case where this assumption failed).

Given the position of the galaxy center (x_c, y_c) , then at a position (x, y) , $dx = x - x_c$ and $dy = y - y_c$, $dx_B = dx * \cos(\theta_B) + dy * \sin(\theta_B)$ $dy_B = (-dx * \sin(\theta_B) + dy * \cos(\theta_B)) / ar_B$ and $r_B^2 = dx_B^2 + dy_B^2$ where θ_B is the position angle of the major axis of the bulge component and ar_B is the axial ratio (minor/major) of the bulge. A similar equation holds for the disk component. The position angles of the two components are allowed to vary independently.

Since the colors of the bulge, disk, and point-source components are expected to be different, the normalisation of the components in each passband were also allowed to vary independently in the fit. However, the structural parameters e.g. orientation, axial ratio and scale length were held fixed for each component across the different passbands.

This gives a maximum of 17 free parameters for each fit, the (x, y) position of the image centre, the relative normalisation of the point source, bulge and disk component in each passband, plus the axial ratio, orientation and scale length of both the bulge and disk components.

For each *BRI* image set, the relative rotation of the detectors used was determined to better than one degree prior to the fitting procedure by comparison of images in each passband. The ground-based frames had rotations near 90 or 180 degrees from each other (i.e. one of the detector axes was always aligned within a few degrees of north) whereas the HST rotation varied continuously and was determined from the position angle of the V3 axis given in the WFPC2 image header.

The fitting was done by minimising χ^2 using a modified Levenberg-Marquardt algorithm. The fitting was typically done over a radius of six arcseconds on both the ground-based and HST images with some variation for individual objects where necessary. The point-source probability was derived using an F-test comparing the value of χ^2 for the best-fit model and the model that fit best without a point source.

We used a relatively large radius in the fitting process primarily to ensure the galaxy model went to zero at large radii. As a result, a significant number of sky pixels that are effectively perfectly fit by the model are included in the calculation of the reduced χ^2 . For some fits, this may bias our estimates of reduced χ^2 value towards lower values.

The fitting procedure is difficult and complex because the general models have three concentric components (bulge, disk, point source) which may, for some parameter values, be similar in shape and size. Thus there is a high degree of correlation between these parameters. In other words, there may be long, flat-bottomed valleys in the χ^2 surface where various combinations of bulge, disk and point source are equally good fits. The correlations will be greatly reduced when the galaxy components are much larger than the point-spread function and/or when the galaxy components have axial ratios much different from unity. In order to ensure that we fit models that are minimal in the sense that they contain the smallest number of components consistent with a good fit to the data, we performed fits of pure disk, pure bulge, bulge-plus-disk, disk-plus-point, bulge-plus-point, bulge-plus-disk-plus-point, and pure point-source models. The models and residuals were examined and the minimal model that was a good fit was accepted.

3.2 Errors

The errors on the 17 parameters in each individual fit can be estimated from the correlation matrix, but such errors are unreliable since there are strong correlations between the errors in different parameters (e.g. between the amplitudes of the point source and bulge components). An estimate of the errors can be made using simulations. The fitted galaxy parameters can be adopted as a starting point and the measured parameters can be varied to produce a range of input models. The results given here provide an indication of the reliability of the fitting results but are not a complete analysis of the problem. The present work is focussed on estimating the errors on the point source versus host galaxy luminosities.

Sets of images were produced with identical object parameters (point source magnitude, galaxy magnitude and morphology) as the selected galaxies in the sample. The objects were simulated in the same (two or three) bands as

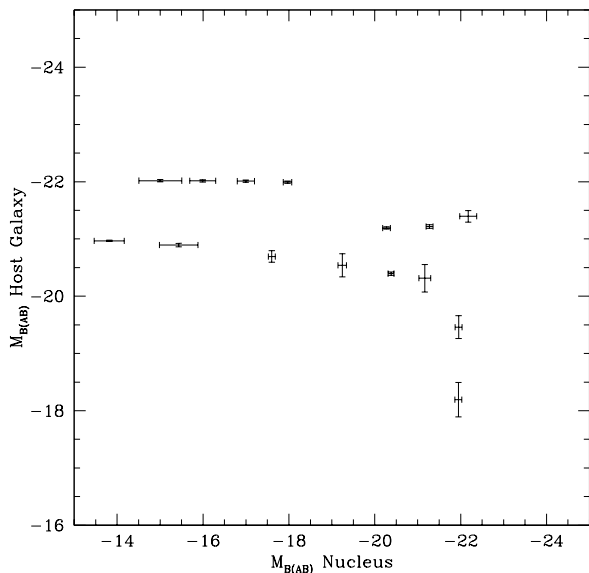


Figure 3 The errors in $M_{B(AB)}$ for nuclear and bulge components derived from the fits to simulated galaxies. Errors include both statistical errors of the fitting process and systematic errors due to the entire processing and fitting procedure (see text). All of the simulations are restricted to bulge-plus-point source models.

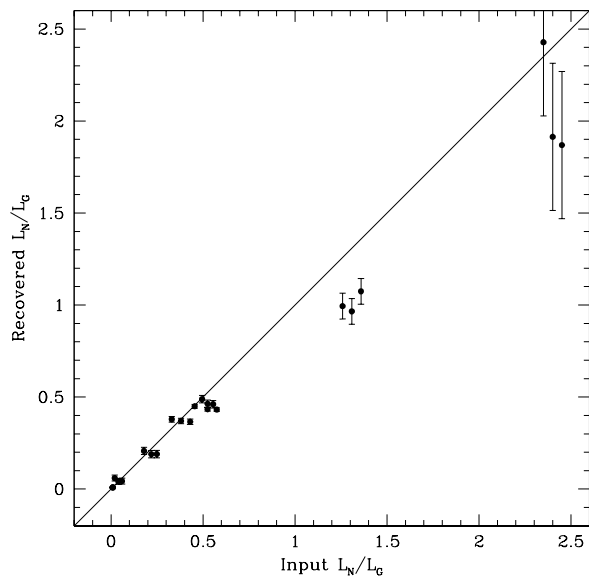


Figure 4 Recovered nuclear-to-host galaxy I-band luminosity ratios (L_N/L_G) compared to input values from the simulations. Errors represent the spread in the recovered L_N/L_G values for a number of different simulations with the same input values.

the observations and convolved with the appropriate PSF. We derived the number of counts from the magnitude and integration times for the real observations. We also set the sky levels and noise in the simulated frames to values typical of those measured in blank regions of the HST and ground-based images. We did, however, make the simplifying assumption that the simulated data frames has been perfectly

flat-fielded. Poisson errors were assumed throughout.

After the actual measured parameters were simulated, some of the parameters were varied to produce a range of simulated object properties. In total 1400 galaxies with 27 different combinations of parameters and PSFs were simulated and fit. The simulations were limited to bulge-plus-point source models because many of the objects are in that class and also because this is a challenging case in terms of disentangling the two most compact components. The only shortcut that was adopted was the use of fitting regions of about three arcseconds as opposed to the six arcsecond regions use for the real data. This was done to save computing time but simulations with varying size of the fitting region shows that this may contribute to systematic errors in the galaxy properties in some cases. A more complete analysis of the errors would require a larger fitting radius.

A simulation requires an input point-spread function for each observation. The PSFs for ground-based observations were always derived from multiple stars on the same frame as the observation itself and thus are accurate and reliable. On the other hand, the HST observations rarely had suitable PSF stars on the image itself and so a single PSF derived from several bright stars on the PC chip was used for all of the fits. This PSF was used to construct all of the simulations but the fitting of the simulations used this same PSF and also two other PSFs that were constructed from the few AGN snapshot frames where stars were available. Thus we can estimate the contribution to the errors that is due to an imperfect knowledge of the PSF.

Fig. 3 shows the results of the simulations and the associated errors in the $M_{B(AB)}(\text{nucleus}) - M_{B(AB)}(\text{host})$ plane. The errors in the photometry produced by the fitting process are dominated by systematic errors in the shape and normalization of the PSF, rather than by statistical errors or sky subtraction. This is because the signal-to-noise ratio of the observations is high. Typical errors near the centroid of the distribution of actual objects in this plane are 5-10 per cent in the magnitudes of the nucleus and host galaxy. As expected, errors in the galaxy magnitude are large where the object is dominated by the nucleus and vice versa. Near $[M_{B(AB)}(\text{nucleus}); M_{B(AB)}(\text{host})] = [-22, -18]$ the corresponding errors are [2 per cent, 10 per cent] whereas near $[-15, -22]$ the errors are [50 per cent, 2 per cent]. Even when nuclear light dominates it is still possible to detect faint ($M_{B(AB)} \sim -18$) host galaxies. Conversely, faint nuclei can be detected in bright ($M_{B(AB)} \sim -22$) host galaxies.

Fig. 4 shows a comparison of input and recovered values of the ratio of I-band nuclear-to-host galaxy luminosity (L_N/L_G). The simulations indicate that low L_N/L_G values are recovered to within a few per cent by the fitting method. On the other hand, objects which are dominated by a strong point source ($L_N/L_G > 1$) may be subject to systematic errors in the sense that the contribution of the nuclear component may be underestimated. As demonstrated below, our HST sample contains relatively few objects with $L_N/L_G > 1$ so that this effect does not significantly affect our results.

Histograms of the recovered values for L_N/L_G for two different input ratios (0.38 and 1.318) are shown in Fig. 5. Separate histograms are shown for each PSF used in the fitting process. This demonstrates that the errors due to PSF

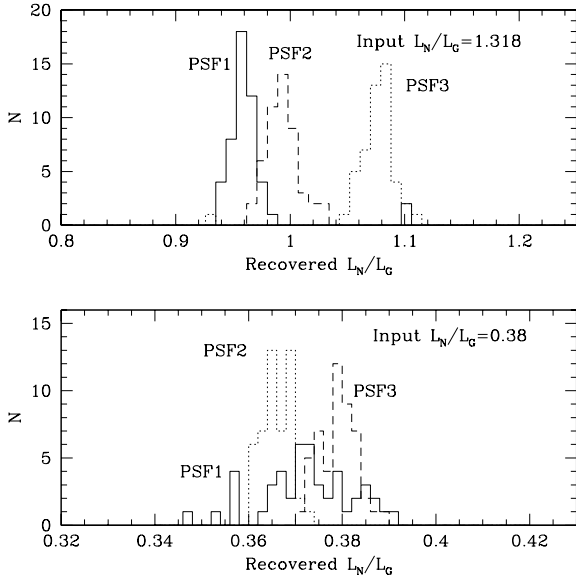


Figure 5 Histograms of recovered nuclear-to-host luminosity ratios (L_N/L_G) for the three different point-spread-functions used in the fitting process. Upper panel: Input $L_N/L_G = 1.318$; lower panel: Input $L_N/L_G = 0.38$.

uncertainty (measured by the shifts between the individual histograms) are significantly larger than the statistical errors of the fitting process (measured by the intrinsic width of individual histograms). For high input values of L_N/L_G , the systematic errors are approximately 25 per cent; for lower values of L_N/L_G the systematic errors reduce to 2 – 3 per cent.

These simulations indicate that the errors derived from the correlation matrix are too small by a factor that varies with the input parameters but is typically a few or more. Those errors are not reliable for multiple component fits (although they are normally good for single component fits). The actual errors for data with a very high signal-to-noise ratio (such as the present case) are dominated by systematic errors due to uncertainty in the point-spread function used in the fitting process. Variations in PSF shape and errors in normalization both contribute to this problem. The actual errors for a particular galaxy depend on the relative contributions of the galaxy and nuclear components (see Fig. 3).

When combining data of varying image quality, there is also the concern that the inclusion of lower (ground-based) resolution data may degrade the fit at the smallest scales, in particular compromising measurement of the nuclear (point source) and/or bulge component. For the 69 AGN in the sample with both HST and ground-based imaging, we therefore compared the nuclear and bulge I -band magnitudes derived from fits to the full (HST + ground-based) data set and to the HST data alone. The comparison between the nuclear/total galaxy I band flux ratio (N/T) obtained from the fits to these two different data-sets is shown in Fig. 6a). A similar comparison for the I band bulge/total galaxy flux ratio (B/T) is shown in Fig. 6b).

For the vast majority of the sample, the derived I -band magnitudes for both nuclear and bulge components

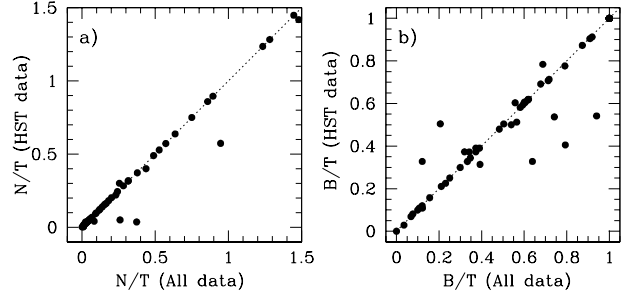


Figure 6 a) I -band nuclear/host galaxy luminosity ratios (N/T) for fits to the HST images only and fits to both ground-based and HST images. b) As Fig. 6a), for I -band bulge-to-total host galaxy luminosity ratio (B/T).

are largely unaffected by inclusion of the ground-based data in the fit. A least squares fit to the relation in Fig. 6a) gives a slope of 1.000 with an rms deviation of 0.067. There are only three cases (MS0721.2+6904, MS1217.0+0700 and MS1306.1–0115) where N/T varies between the fits by greater than this value. Removal of these three points reduces the rms to 0.015, smaller than systematic errors inherent in the fitting process due to the PSF.

The relation between the different B/T estimates shows a larger scatter, $\sigma(B/T) = 0.092$, dominated by six AGN whose B/T values which differ by greater than 0.1 between the fits. Removal of these objects from the comparison reduces the observed scatter to $\sigma(B/T) = 0.02$, again below the level of the systematic errors introduced by the PSF fitting.

However, even the presence of small numbers of objects in our sample with potentially large uncertainties in their B/T values ($\Delta(B/T) > 0.1$) have little effect on the results presented below. In this paper, we use the B/T ratio largely to conduct an quantitative (albeit crude) morphological classification of the host galaxy. Independent visual classification of the host galaxies confirm that the B/T values derived from the joint HST/ground-based data-set yield accurate morphological types. If we were to use the B/T values derived from the HST data alone to carry out the morphological classification this would only change the type assigned to four AGN host galaxies – a net change over the entire sample of 1 less elliptical, 3 more Sab and 2 less Sbc galaxies.

We conclude that the overall effect of simultaneously fitting to the full imaging data-set provides useful additional constraints on the overall parameters of the fits, without systematically biasing the estimates of nuclear or bulge properties. In a small fraction of AGN (5 – 10 per of the total sample) there are differences between the derived nuclear/bulge luminosities with/without the inclusion of ground-based data. However, these are at level which do not significantly affect any of our conclusions drawn below. Indeed, there is no reason to believe that fits to the HST data alone necessarily produce more accurate estimates of the bulge and/or nuclear properties. By neglecting the ground-based data we may be poorly fitting the low surface brightness disk, biasing the derived properties for the bulge and/or point source component.

4 RESULTS

4.1 Observed Properties of the sample

The results of the fitting procedure are listed in Table 2. This table lists 11/17 free parameters in the fit including the fitted B , R and I AB magnitudes for the point source, bulge and disk components for each AGN. The ratio of bulge-to-total light in the I passband (B/T) is also given, together with the bulge (R_e) and disk (h) radii. We also give the reduced χ^2 for the fit and the probability (P_{PS}) that a point source is not required by the fit.

Ten objects imaged in this survey show little evidence for a point source component: $P_{\text{PS}} = 1$. Of these, only two (MS0039.0-0145 and MS1114.4+1801) are ‘ambiguous’ AGN as identified by Stocke et al. (1991). This leaves eight objects, or approximately ten per cent of the sample, which have been classified as broad emission-line AGN but have no detectable nuclear component. It is possible that these objects were incorrectly classified as broad-emission line AGN in the EMSS, despite the care taken to flag all potentially ambiguous cases. Although no cases were found of an AGN without a detectable point source in any of the HST imaging survey of bright ($M_B < -23$) AGN (Bachall et al. 1997, Boyce et al. 1997, McLure et al. 1999), in an HST imaging study of 91 Seyfert 1 galaxies, Malkan et al. (1998) find an even greater percentage (~ 35 per cent) of broad emission line AGN that exhibit no evidence of any point source component. Malkan et al. (1998) ascribe this to dust absorption of the central source. It could be argued that the amount of dust required to obscure the central regions under these circumstances would also extinguish the broad line region, the basis on which these objects were classified as AGN. Of course, the obscuration may be patchy and the nucleus may have become obscured since its spectroscopic classification as a broad lined AGN. Equally, these objects may not even harbour a compact point source; the broad lines created by intense star formation in the central regions of the galaxy (see e.g. Terlevich et al. 1992). Whatever the origin, the results from the current HST surveys appear to indicate a trend for an increasing fraction of AGN with no point source component with decreasing AGN luminosity.

At the opposite extreme, we do not find any cases where there is no evidence for a host galaxy. In the case of MS1020.2+6850, HST imaging shows evidence for a weak disk only but both B and R -band images show a luminosity profile that is significantly more extended than the PSF.

Good fits ($\chi^2 \leq 2$) were obtained for the vast majority of the AGN in this analysis. Although the large fitting radius may bias estimates of χ^2 towards low values (see above), visual examination of all residual (data – model) images confirmed that no significant systematic effects remained after the model fitting process. The largest reduced χ^2 residual ($\chi^2 = 4.2$) was found for the fit to MS0754.6+3928. Visual inspection of this object clearly reveals a strong point source component and a low surface brightness disk.

Fig. 7 shows the observed $(B - I)_{\text{AB}}$ colour histograms for the point source, bulge and disk components. The mean fitted $(B - I)_{\text{AB}}$ colour for the point source component is significantly bluer, $(B - I)_{\text{AB}} = 0.2$, than that derived for the disk or bulge components, $(B - I)_{\text{AB}} = 1.2$. These colours are consistent with previous observations of QSOs

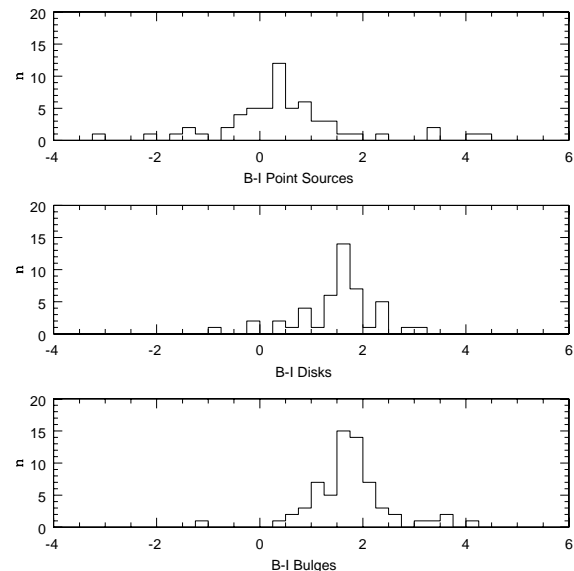


Figure 7 $(B - I)_{\text{AB}}$ histogram for the point source, bulge and disk components.

and galaxies, and thus provide a useful consistency check on the fitting procedure since no a priori assumptions were fed into the fit relating to the colour of the components.

Although the $(B - I)_{\text{AB}}$ colour distribution for the galaxy components are reasonably tight ($\sigma = 0.3$ mag), there is a long tail to both blue and red in the $(B - I)_{\text{AB}}$ colour distribution for point sources. This is an artifact caused by the fitting procedure. Where the point source is weak and/or the ground-based B data is poor, the B fit is poorly constrained, resulting in large errors. For this reason, we chose not to use B band magnitudes obtained from the fit to compute derived rest-frame absolute magnitudes for point sources in the $M_{B(\text{AB})}$ band. Instead we used the mean point source $(B - I)_{\text{AB}}$ colour to transform the I -band HST fits to the B passband. For the galaxy components we used the fitted B - or R -band magnitudes, unless there were no ground-based data in the relevant band. In that case, the median colour for the component was used.

The absolute $M_{B(\text{AB})}$ magnitudes for all three components derived in this manner are given in Table 3, along with the physical sizes for the disk and bulge components. For completeness, the monochromatic X-ray, radio and optical fluxes (at 2keV, 5GHz and 2500Å respectively) of the point source component are also given. To derive the radio and X-ray luminosities we have assumed spectral indices of $\alpha_R = 0.5$ and $\alpha_X = 1$ in the radio and X-ray regimes. We have also assumed that all the radio and X-ray flux comes from the central component.

4.2 Host Galaxy Properties

4.2.1 Luminosity

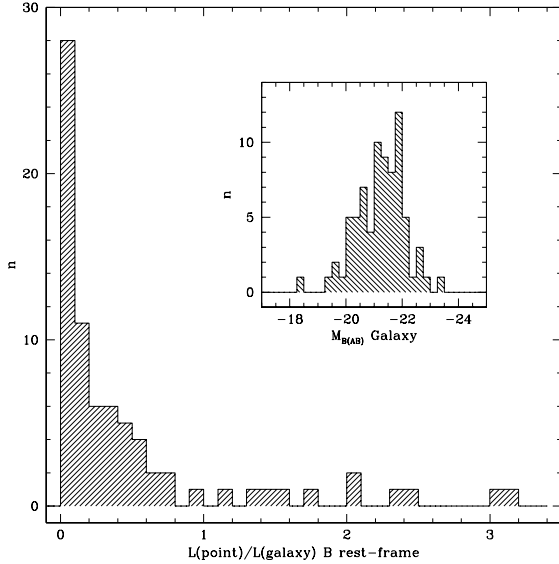
The histogram of host galaxy luminosities (corrected to the rest-frame $B(\text{AB})$ pass-band) is plotted in Fig. 8. The luminosity range of the host galaxies is $-23.1 < M_{B(\text{AB})} <$

Table 2. Fitted parameters for AGN/Host Galaxies

Name	$B(AB)$	Point $R(AB)$	$I(AB)$	$B(AB)$	Bulge $R(AB)$	$I(AB)$	$B(AB)$	Disk $R(AB)$	$I(AB)$	B/T	R_e ($''$)	h ($''$)	χ^2	P_{PS}
MS0007.1–0231	19.00	—	19.01	19.75	—	16.59	17.53	—	15.84	0.33	0.68	1.92	0.74	0.00
MS0039.0–0145	—	—	—	19.10	—	17.07	20.60	—	17.63	0.63	0.70	3.13	0.75	1.00
MS0048.8+2907	16.78	17.21	20.01	16.79	14.79	14.11	17.89	16.42	16.14	0.87	3.02	2.26	0.58	0.00
MS0111.9–0132	18.76	—	18.45	18.30	—	16.52	—	—	—	1.00	8.42	—	0.80	0.00
MS0135.4+0256	—	—	—	18.32	18.00	16.81	18.92	17.88	16.98	0.54	1.66	4.35	0.90	1.00
MS0144.2–0055	—	—	18.04	—	—	19.13	—	—	15.30	0.03	0.37	2.57	0.62	0.00
MS0321.5–6657	—	—	—	18.62	—	16.87	19.29	—	17.15	0.56	0.82	2.64	0.68	1.00
MS0330.8+0606	20.10	19.86	19.69	26.70	18.68	17.55	18.38	17.13	16.73	0.32	1.50	3.05	0.76	0.00
MS0340.3+0455	28.17	27.08	20.75	21.95	20.04	19.25	18.21	17.15	16.42	0.07	0.45	2.59	0.67	0.56
MS0412.4–0802	15.84	15.11	14.89	16.79	15.48	15.16	—	—	—	1.00	3.35	—	1.59	0.00
MS0444.9–1000	20.71	21.92	20.40	19.89	18.23	17.82	18.43	17.30	17.10	0.34	0.63	2.75	0.80	0.41
MS0457.9+0141	19.47	—	19.39	18.08	—	16.19	—	—	—	1.00	4.94	—	0.78	0.00
MS0516.6–4609	—	—	—	—	—	15.00	—	—	14.30	0.34	5.69	17.06	0.36	1.00
MS0713.4+3700	19.77	19.59	20.88	17.32	16.17	15.47	—	—	—	1.00	2.57	—	0.52	0.00
MS0719.9+7100	17.85	18.20	17.56	18.60	17.29	16.86	—	—	—	1.00	1.44	—	0.83	0.00
MS0721.2+6904	18.11	17.26	17.31	19.13	19.19	17.32	20.17	18.28	20.30	0.94	1.49	1.96	0.85	0.00
MS0731.6+8011	27.46	19.67	19.07	17.46	16.06	15.63	—	—	—	1.00	2.56	—	0.62	0.00
MS0754.6+3928	15.35	17.17	14.22	16.71	18.44	15.56	—	—	—	1.00	1.59	—	4.22	0.00
MS0801.9+2129	16.24	17.30	16.46	18.86	17.00	17.60	18.08	16.82	16.68	0.30	0.64	1.79	1.00	0.00
MS0803.3+7557	18.32	17.95	17.40	17.28	15.86	15.71	18.64	18.26	17.15	0.79	6.27	1.37	0.60	0.00
MS0818.8+5428	18.38	17.52	18.66	17.67	17.67	16.52	21.85	17.86	18.61	0.87	0.65	1.67	0.81	0.00
MS0841.7+1628	20.34	19.31	18.53	19.83	18.52	17.93	—	—	—	1.00	1.32	—	0.64	0.00
MS0842.7–0720	17.08	17.33	17.26	20.62	17.50	17.22	18.42	17.09	16.75	0.39	1.61	3.01	0.67	0.00
MS0844.9+1836	19.61	18.76	21.06	17.97	16.81	16.43	19.11	17.27	17.42	0.71	1.01	2.32	0.50	0.24
MS0849.5+0805	15.52	—	16.39	14.91	—	15.10	—	—	—	1.00	3.85	—	0.58	0.00
MS0904.4–1505	18.19	18.84	18.71	17.78	15.86	15.73	19.10	19.31	18.22	0.91	3.20	1.21	0.53	0.00
MS0905.6–0817	18.59	17.71	18.50	18.10	17.09	16.46	17.62	16.37	15.90	0.37	1.65	4.48	0.41	0.00
MS0942.8+0950	18.57	18.34	18.43	17.88	16.50	16.17	16.45	15.46	14.97	0.25	3.12	2.12	0.73	0.00
MS0944.1+1333	15.68	15.70	16.06	17.33	18.98	16.68	18.97	17.25	16.70	0.50	0.25	1.50	1.10	0.00
MS1020.2+6850	20.77	17.75	17.48	—	—	—	17.89	18.56	17.90	0.00	—	2.66	0.89	0.00
MS1058.8+1003	18.96	18.14	21.03	16.00	15.11	14.49	22.78	15.25	15.02	0.62	2.01	9.63	0.46	0.12
MS1059.0+7302	17.57	17.22	17.03	18.09	17.41	15.87	18.16	17.11	17.02	0.74	3.47	2.16	0.55	0.00
MS1108.3+3530	—	—	—	17.24	16.07	16.03	18.89	16.29	15.95	0.48	1.06	2.52	0.54	1.00
MS1110.3+2210	22.12	19.59	20.41	17.41	15.65	15.50	18.70	18.86	18.13	0.92	2.86	0.74	0.52	0.64
MS1114.4+1801	—	—	—	18.06	16.96	16.57	19.93	17.88	17.58	0.72	1.03	2.74	0.68	1.00
MS1136.5+3413	17.23	16.86	16.82	16.81	17.15	16.16	17.87	15.75	15.59	0.37	3.83	4.18	0.95	0.00
MS1138.1+0400	19.77	19.40	19.33	18.18	17.33	16.81	—	—	—	1.00	0.96	—	0.87	0.00
MS1139.7+1040	19.00	19.45	19.29	22.42	21.24	18.31	18.46	17.28	16.85	0.21	1.23	3.12	0.74	0.00
MS1143.5–0411	—	—	17.71	—	—	17.49	—	—	16.67	0.32	2.63	2.06	0.72	0.00
MS1158.6–0323	20.19	16.16	17.72	16.74	16.92	15.98	16.35	14.59	14.67	0.23	2.03	2.51	0.35	0.00
MS1200.1–0330	27.70	19.59	19.65	17.70	16.83	16.01	24.69	16.62	16.37	0.58	1.51	2.05	0.69	0.78
MS1205.7+6427	18.70	18.79	18.31	19.47	18.72	17.62	18.93	18.41	18.04	0.59	1.98	0.83	0.75	0.00
MS1214.3+3811	20.95	18.45	20.47	18.25	19.09	17.92	17.32	16.02	15.63	0.11	0.25	3.49	0.82	0.49
MS1217.0+0700	17.79	17.57	16.95	19.85	17.95	18.17	17.35	16.25	16.02	0.12	1.76	1.38	0.65	0.00
MS1219.6+7535	19.83	18.42	15.74	16.36	14.96	15.49	15.13	13.72	16.00	0.62	2.30	3.40	1.71	0.00
MS1220.9+1601	21.39	18.58	19.95	17.82	16.91	16.40	17.81	17.27	17.02	0.64	2.41	1.19	0.49	0.00
MS1232.4+1550	17.00	16.84	17.72	19.89	16.69	16.35	14.55	12.90	12.76	0.04	0.72	15.90	0.58	0.00
MS1233.3+7426	—	—	—	19.01	18.43	17.88	17.41	15.93	15.48	0.10	0.25	3.21	2.02	1.00
MS1239.2+3219	18.97	18.13	18.34	20.51	20.33	18.03	18.21	17.01	16.60	0.21	0.93	1.96	0.84	0.00
MS1242.2+1632	—	—	—	19.48	18.74	18.25	17.48	16.27	16.10	0.12	0.25	3.15	0.62	1.00
MS1306.1–0115	19.87	19.75	18.85	19.49	17.66	17.39	—	—	—	1.00	0.95	—	0.83	0.00
MS1322.3+2925	19.44	—	20.97	18.31	—	17.12	—	—	—	1.00	0.85	—	0.63	0.33
MS1327.4+3209	18.51	18.90	18.00	17.94	16.56	16.38	17.87	17.08	16.91	0.62	2.02	4.85	1.18	0.00
MS1333.9+5500	18.13	18.28	17.48	20.76	17.63	17.13	18.53	17.34	16.65	0.39	2.32	2.17	0.76	0.00
MS1334.6+0351	20.12	19.44	19.85	18.49	17.11	16.46	—	—	—	1.00	3.17	—	0.72	0.00
MS1335.1–3128	21.01	18.88	19.51	18.83	17.81	16.93	—	—	—	1.00	1.63	—	0.95	0.00
MS1351.6+4005	18.91	—	20.30	23.40	—	15.56	17.35	—	17.01	0.79	2.97	1.66	0.44	0.66
MS1403.5+5439	21.02	19.86	19.90	18.16	17.25	16.64	—	—	—	1.00	1.82	—	0.75	0.00

Table 2 contd. Fitted parameters for AGN/Host Galaxies

Name	$B(AB)$	Point $R(AB)$	$I(AB)$	Bulge $B(AB)$	$R(AB)$	$I(AB)$	Disk $B(AB)$	$R(AB)$	$I(AB)$	B/T	R_e (")	h (")	χ^2	P_{PS}
MS1408.1+2617	18.25	18.16	18.30	18.65	17.49	17.06	—	—	—	1.00	1.68	—	0.83	0.00
MS1414.0+0130	19.42	—	19.59	19.83	—	17.74	—	—	—	1.00	1.04	—	0.81	0.01
MS1414.9+1337	—	—	—	19.82	17.97	17.49	19.21	17.24	16.80	0.35	0.77	2.75	0.77	1.00
MS1416.3–1257	17.46	—	16.56	19.24	—	17.33	20.18	—	17.79	0.60	0.81	3.29	0.89	0.00
MS1420.1+2956	17.63	17.24	17.97	19.78	19.70	17.36	16.71	15.57	15.21	0.12	0.39	3.36	0.57	0.00
MS1426.5+0130	18.99	—	14.67	22.14	—	15.08	—	—	—	0.54	3.04	—	1.69	0.00
MS1455.7+2121	19.08	18.54	18.30	17.55	16.57	15.98	—	—	—	1.00	2.86	—	0.58	0.00
MS1456.4+2147	16.88	—	16.65	17.80	—	16.34	—	—	—	1.00	1.93	—	0.57	0.00
MS1519.8–0633	16.82	16.64	16.53	17.17	16.13	16.27	18.21	18.04	16.52	0.56	5.89	2.00	0.96	0.00
MS1545.3+0305	18.29	—	17.92	18.41	—	16.43	18.64	—	16.88	0.60	2.33	2.04	0.66	0.00
MS1846.5–7857	18.77	16.99	18.10	15.88	14.49	13.79	14.98	13.60	14.65	0.69	6.13	20.60	0.77	0.00
MS2039.5–0107	20.19	—	18.75	18.34	—	17.22	—	—	—	1.00	2.16	—	1.02	0.00
MS2128.3+0349	16.83	—	16.50	17.89	—	16.01	—	—	—	1.00	3.05	—	1.10	0.00
MS2144.9–2012	18.94	—	18.84	18.16	—	16.23	18.58	—	17.03	0.68	1.27	2.12	0.67	0.00
MS2159.5–5713	—	—	17.67	—	—	15.47	—	—	18.61	0.95	2.38	2.27	0.49	0.00
MS2210.2+1827	20.79	18.27	17.48	17.66	19.23	18.68	17.53	16.50	15.98	0.08	0.28	2.27	0.58	0.00
MS2348.3+3250	19.41	—	18.85	20.79	—	17.32	—	—	—	1.00	0.97	—	0.93	0.15
MS2348.6+1956	—	—	—	18.46	17.53	16.93	16.72	15.52	15.10	0.16	0.23	2.45	1.00	1.00

**Figure 8** Histogram of nuclear-to-host luminosity ratio for the sample. (Inset: Host galaxy luminosity histogram).

–18.3 with a median value of $M_{B(AB)} = -21.1$. The mean value for the I -band nuclear-to-host luminosity ratio (also plotted in Fig. 8) is $L_N/L_G = 0.2$, lower than that observed in previous samples of bright AGN. Over 75 per cent of our sample exhibit $L_N/L_G < 0.5$. In contrast, McLure et al. (1999) obtain a median R -band value $L_N/L_G = 1.5$ from their sample of nine radio-quiet AGN. At the low L_N/L_G measured in this sample, any systematic effects introduced by the fitting procedure are, at most, at the 2–3 per cent level (see section 3.2). We conclude, therefore the low values for L_N/L_G found here are unlikely to be artifact of the fitting procedure.

To establish whether the properties of the AGN host galaxies were representative of the field galaxy population, we tested the luminosity distribution of the host galaxies in this sample against a control sample of galaxies from the Autofib redshift survey (Ellis et al. 1996). For each AGN host galaxy, ten galaxies with the same apparent magnitude (± 0.05 mag) were chosen at random and with replacement from the Autofib sample. A small random offset ($-0.01 < \delta z < 0.01$) was applied to each redshift in the Autofib sample to minimise the effects of clustering in this sample. If the luminosity distributions of the randomly-drawn Autofib sample and the AGN host sample are identical then we would expect the redshift distributions of the two samples to match one another. A Kolmogorov-Smirnov (K-S) test shows that the distributions are different at greater than the 99.9 per cent significance level (see Fig. 9a). The sense of the difference is that the AGN hosts are displaced toward higher redshifts, implying the hosts are more luminous than typical field galaxies as represented by the Autofib sample. By applying increasingly large magnitude offsets to the galaxies drawn at random from the Autofib sample, we were able to establish that the AGN hosts were brighter by 0.75 ± 0.25 mag at the 95 per cent confidence level than the Autofib galaxies.

4.2.2 Morphology

The morphological types can be characterised according to the output parameters of the fitting procedure. In this scheme the fractional bulge luminosity B/T is the primary classification parameter. We approximately follow Simien & de Vaucouleurs (1986) and define the E/S0 class with $0.5 \leq B/T < 1.0$, Sab; $0.3 \leq B/T < 0.5$, Sbc; $0.1 \leq B/T < 0.3$, and we define our own ‘Late’ class as $B/T < 0.1$. Fig. 10a) plots the histogram of the rest-frame B-band values of B/T computed using the median $(B - I)_{AB}$ galaxy colors.

An alternative method is to visually classify the images roughly according to the Hubble classification system.

Table 3. Derived parameters for AGN/Host Galaxies

Name	$M_{B(AB)}(\text{Point})$	$M_{B(AB)}(\text{Bulge})$	$M_{B(AB)}(\text{Disk})$	$\log(L_{2\text{keV}})$	Point $\log(L_{5\text{GHz}})$	$\log(L_{2500\text{\AA}})$	$\log[R_e(\text{kpc})]$	$\log[h(\text{kpc})]$
MS0007.1-0231	-19.10	-19.58	-21.52	25.62	29.64	28.20	0.17	0.62
MS0039.0-0145	—	-20.73	-20.15	25.21	29.64	—	0.27	0.92
MS0048.8+2907	-16.17	-20.20	-19.01	25.66	29.03	27.03	0.47	0.35
MS0111.9-0132	-20.36	-21.58	—	25.62	30.14	28.71	1.38	—
MS0135.4+0256	—	-22.00	-21.62	25.77	29.86	—	0.75	1.17
MS0144.2-0055	-19.88	-17.96	-21.77	25.36	29.36	28.52	-0.13	0.72
MS0321.5-6657	—	-20.61	-20.11	25.29	—	—	0.28	0.79
MS0330.8+0606	-18.83	-13.01	-21.11	25.62	29.54	28.09	0.58	0.89
MS0340.3+0455	-17.60	-18.27	-21.08	25.05	29.53	27.60	0.03	0.79
MS0412.4-0802	-21.35	-20.15	—	25.32	29.06	29.10	0.53	—
MS0444.9-1000	-17.90	-19.54	-20.66	25.12	29.39	27.72	0.17	0.81
MS0457.9+0141	-19.56	-22.02	—	26.12	29.78	28.39	1.17	—
MS0516.6-4609	—	-20.94	-21.62	25.08	31.00	—	0.86	1.34
MS0713.4+3700	-17.97	-22.64	—	25.70	29.78	27.75	0.87	—
MS0719.9+7100	-21.35	-21.37	—	25.85	29.75	29.10	0.63	—
MS0721.2+6904	-21.33	-20.57	-18.94	26.05	29.65	29.10	0.60	0.72
MS0731.6+8011	-19.04	-21.65	—	25.99	29.48	28.18	0.75	—
MS0754.6+3928	-24.10	-22.36	—	25.99	30.15	30.20	0.58	—
MS0801.9+2129	-22.32	-20.75	-21.58	25.85	29.80	29.49	0.25	0.70
MS0803.3+7557	-20.88	-21.90	-20.50	25.85	29.50	28.92	1.17	0.51
MS0818.8+5428	-19.42	-21.13	-17.44	25.73	29.60	28.33	0.15	0.56
MS0841.7+1628	-20.77	-20.69	—	25.87	29.92	28.87	0.65	—
MS0842.7-0720	-21.95	-20.13	-21.88	25.88	29.88	29.35	0.73	1.00
MS0844.9+1836	-17.02	-20.99	-19.91	25.60	29.30	27.37	0.34	0.70
MS0849.5+0805	-20.97	-21.42	—	26.35	28.93	28.95	0.80	—
MS0904.4-1505	-18.35	-20.20	-18.58	25.24	29.06	27.90	0.66	0.24
MS0905.6-0817	-19.16	-20.42	-20.93	25.30	29.13	28.23	0.48	0.91
MS0942.8+0950	-15.52	-16.66	-18.07	24.60	27.64	26.77	0.06	-0.11
MS0944.1+1333	-22.95	-22.28	-21.37	26.60	30.34	29.74	-0.12	0.66
MS1020.2+6850	-20.39	—	-20.47	25.00	29.21	28.72	—	0.72
MS1058.8+1003	-14.60	-20.26	-13.51	24.31	29.30	26.40	0.19	0.87
MS1059.0+7302	-21.13	-21.22	-20.73	25.79	29.45	29.01	0.89	0.68
MS1108.3+3530	—	-20.76	-19.46	25.06	29.75	—	0.23	0.61
MS1110.3+2210	-15.37	-19.08	-17.60	24.42	28.71	26.71	0.38	-0.22
MS1114.4+1801	—	-21.03	-19.51	24.70	29.36	—	0.37	0.80
MS1136.5+3413	-19.10	-19.64	-18.81	25.45	28.43	28.20	0.53	0.56
MS1138.1+0400	-19.04	-21.01	—	25.20	29.48	28.18	0.37	—
MS1139.7+1040	-20.02	-18.33	-21.91	26.21	30.27	28.57	0.62	1.03
MS1143.5-0411	-21.33	-20.75	-21.54	25.98	29.86	29.10	0.91	0.81
MS1158.6-0323	-17.17	-18.69	-19.16	25.16	28.35	27.43	0.06	0.15
MS1200.1-0330	-17.82	-20.62	-13.70	24.76	29.61	27.69	0.41	0.54
MS1205.7+6427	-20.21	-20.11	-20.28	25.58	30.00	28.65	0.71	0.33
MS1214.3+3811	-16.89	-19.62	-20.89	24.99	29.18	27.32	-0.39	0.75
MS1217.0+0700	-20.97	-18.98	-21.34	25.51	29.36	28.95	0.55	0.45
MS1219.6+7535	-21.92	-21.94	-23.01	26.49	29.43	29.33	0.62	0.79
MS1220.9+1601	-18.00	-20.93	-20.77	25.41	29.47	27.77	0.69	0.39
MS1232.4+1550	-18.99	-17.67	-22.96	25.33	28.87	28.16	-0.05	1.29
MS1233.3+7426	—	-19.74	-21.65	25.07	29.40	—	-0.28	0.83
MS1239.2+3219	-18.68	-17.48	-19.58	24.87	29.00	28.03	0.12	0.44
MS1242.2+1632	—	-19.37	-21.43	25.85	29.71	—	-0.26	0.84
MS1306.1-0115	-19.79	-20.34	—	25.48	29.70	28.48	0.41	—
MS1322.3+2925	-16.72	-20.08	—	25.09	29.27	27.25	0.20	—
MS1327.4+3209	-20.18	-21.13	-21.01	25.53	30.30	28.64	0.66	1.04
MS1333.9+5500	-21.08	-19.07	-21.11	25.73	29.71	29.00	0.78	0.75
MS1334.6+0351	-19.24	-21.84	—	25.50	29.77	28.26	1.00	—
MS1335.1-3128	-18.46	-20.16	—	25.07	29.32	27.95	0.53	—
MS1351.6+4005	-17.07	-14.87	-20.51	25.25	29.23	27.39	0.68	0.43
MS1403.5+5439	-18.08	-20.67	—	25.26	29.38	27.80	0.58	—

Table 3 contd. Derived parameters for AGN/Host Galaxies

Name	$M_{B(AB)}(\text{Point})$	$M_{B(AB)}(\text{Bulge})$	$M_{B(AB)}(\text{Disk})$	$\log(L_{2\text{keV}})$	Point $\log(L_{5\text{GHz}})$	$\log(L_{2500\text{\AA}})$	$\log[R_e(\text{kpc})]$	$\log[h(\text{kpc})]$
MS1408.1+2617	-19.39	-19.89	—	25.19	29.27	28.32	0.49	—
MS1414.0+0130	-19.60	-20.64	—	25.91	29.97	28.40	0.53	—
MS1414.9+1337	—	-19.49	-20.12	25.05	29.44	—	0.23	0.78
MS1416.3-1257	-22.42	-20.89	-20.16	26.76	29.78	29.53	0.39	1.00
MS1420.1+2956	-19.05	-18.19	-21.05	25.06	29.05	28.18	-0.26	0.68
MS1426.5+0130	-23.41	-22.18	—	26.36	29.67	29.93	0.82	—
MS1455.7+2121	-19.62	-21.25	—	25.64	29.41	28.41	0.76	—
MS1456.4+2147	-20.71	-20.33	—	25.44	29.23	28.85	0.50	—
MS1519.8-0633	-21.47	-21.51	-20.72	25.95	30.24	29.15	1.09	0.62
MS1545.3+0305	-20.45	-21.06	-20.73	25.58	29.54	28.74	0.75	0.69
MS1846.5-7857	-17.61	-20.55	-21.22	24.79	—	27.61	0.69	1.22
MS2039.5-0107	-20.43	-21.70	—	25.63	29.81	28.74	0.85	—
MS2128.3+0349	-21.78	-21.43	—	26.09	29.50	29.28	0.85	—
MS2144.9-2012	-19.61	-21.38	-20.79	25.54	29.62	28.41	0.50	0.73
MS2159.5-5713	-20.34	-21.71	-18.54	25.66	31.48	28.70	0.70	0.68
MS2210.2+1827	-20.42	-20.73	-21.23	25.75	29.35	28.73	-0.25	0.66
MS2348.3+3250	-19.33	-20.03	—	25.54	29.56	28.29	0.34	—
MS2348.6+1956	—	-18.77	-20.58	24.82	29.25	—	-0.57	0.45

We used the Hubble Atlas (Sandage 1961) as a reference. One difficulty with this approach is that some of the objects in this sample are dominated by a nuclear component so that estimating the contribution of the bulge is problematical. The bulge and nuclear light are easily confused. This problem was dealt with by subtracting the point source component from the best-fit model and then re-evaluating the classifications. The affect of this re-evaluation was negligible. However, nine galaxies were very compact and/or dominated by the nuclear contribution so that it was not possible to classify them with any degree of confidence. All of these objects were classified as ‘Late’ for the purposes of the comparisons below. A comparison of the distributions of the profile-fitting and visual classification (Figs 10a and b) shows no significant difference.

To test whether these distributions are characteristic of the field galaxy population at these magnitudes, we compared our visual classifications against those from 10 random samples generated from the Autofib survey using the method described above. The resulting histogram of morphological types for the Autofib sample is shown in Fig. 10c). We adopted our visual classifications for the purpose of this comparison since these are likely to be derived in a similar way to those of the Autofib survey. Using only the 4 rough classes defined above, the comparison between the Autofib and AGN host galaxies samples yielded a $\chi^2 = 69$ for 4 degrees of freedom. Clearly the AGN host galaxies are drawn from a different parent population than the general field population. AGN host galaxies in this sample tend to be of earlier type than the field. Remarkably, 55 per cent of the AGN host galaxies are E/S0 type.

This percentage is similar to the fraction of early-type hosts identified amongst bright radio-quiet QSOs ($M_B < -23$) by both Bahcall et al. (1997) and McLure et al. (1999). Bahcall et al. (1997) identified 7 out of 14 of their radio-quiet AGN to have bulge luminosity profiles, while McLure et al. (1999) found elliptical galaxy fits were favoured over disk galaxy fits in seven out of the nine radio-quiet AGN

they studied. Because the disk host galaxies were found preferentially around the low luminosity AGN in their sample, McLure et al. (1999) postulated that early-type hosts may be more prevalent amongst bright AGN. Within the statistical errors, our analysis would suggest that this is not the case; the frequency of early type hosts is almost as high amongst our fainter sample as in the McLure et al. (1999) sample. This observation is also internally consistent within our own sample. Using the Spearman rank test, we find no significant correlation between B/T and point source luminosity (see Fig. 11). A least squares fit to the data points in Fig. 11 formally gives a slope of 0.0. At the very brightest nuclear magnitudes, our statistics are too poor to determine whether AGN inhabit *exclusively* bulge-dominant systems as suggested by McLure et al. We have only two AGN with $M_{B(AB)}(\text{nucleus}) < -23$ in our sample, both of which have $B/T > 0.5$.

In contrast, although Malkan et al. (1998) report that Seyfert 1s have earlier-type host galaxies than Seyfert 2s, the overall fraction of Seyfert 1 galaxies in E/S0 hosts in their HST imaging survey is much lower (~ 20 per cent) than observed in this analysis. Thus the high incidence of early-type hosts for radio quiet AGN may break down at the very lowest AGN luminosities ($M_B > -20$).

The observation that the AGN host galaxies are biased towards earlier types is also consistent with our observation that the absolute magnitudes of the host galaxies are brighter than the field population. Folkes et al. (1999) have recently derived the field galaxy luminosity function for different spectral types in the 2dF galaxy redshift survey. Based on almost 6000 galaxies, they obtain an $M_{B(AB)}^* = -21.2$ for early type galaxies, 0.7 mag brighter than the $M_{B(AB)}^*$ for late-type galaxies. This is close to the median luminosity of the AGN host galaxies in this sample. Furthermore, the difference between the $M_{B(AB)}^*$ derived for early and late-type galaxies in the 2dF survey is close to the observed luminosity difference between the AGN host

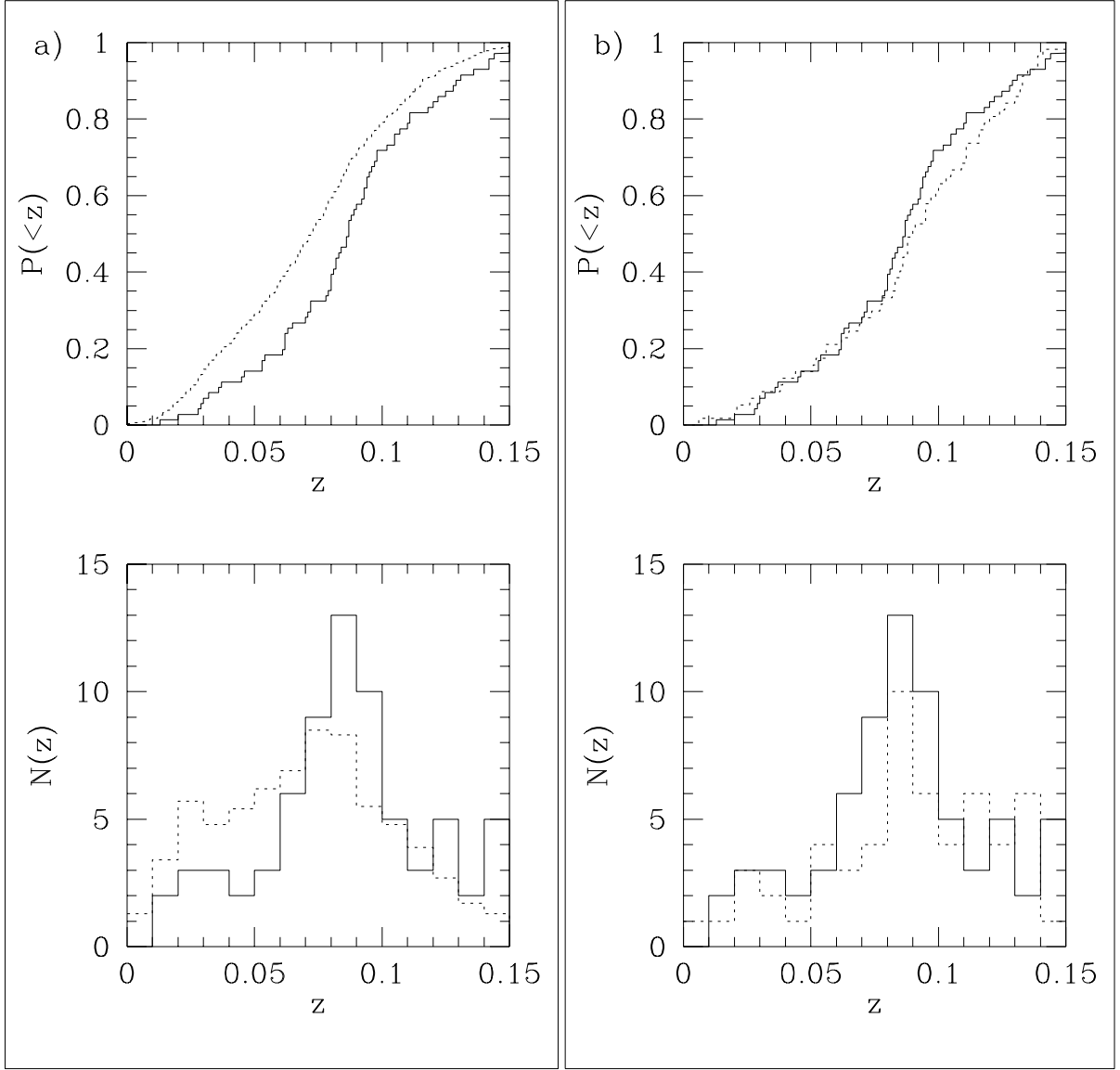


Figure 9 Comparison of redshift distributions for the EMSS sample (solid line) with random-sample drawn from Autofib sample (dotted line) a) Autofib random-sample drawn to match apparent magnitude distribution of EMSS sample b) random-sample drawn to match apparent magnitude and morphological distribution of the EMSS sample. Upper panel: cumulative redshift distribution. Lower panel: redshift histograms.

galaxies and the random field sample.

We performed a variant of the earlier test with the Autofib sample to see whether the luminosity difference is consistent with the galaxies being biased toward earlier spectral types. This time we selected galaxies at random from the Autofib sample with identical apparent magnitudes (± 0.05 mag) and spectral types. Since we were much more restricted in our choice of galaxy from the Autofib sample we were only able to do this test with the same number of objects in the randomly-selected Autofib sample as in the EMSS sample (typically only 1–3 objects had the same apparent magnitude and morphology) as the host galaxies in the EMSS sample. We computed the KS probability for the

two resultant redshift distributions being drawn from the same sample (see Fig. 9b). In this case the KS probability was $P_{KS} = 0.75$, i.e. there is no evidence that the AGN host galaxies in this sample have a different luminosity distribution when compared to the same morphological type distribution in the field. The difference in luminosity between the AGN host galaxies and the random field galaxy population is therefore a natural consequence of the bias towards earlier type galaxies in this population.

4.2.3 Sizes

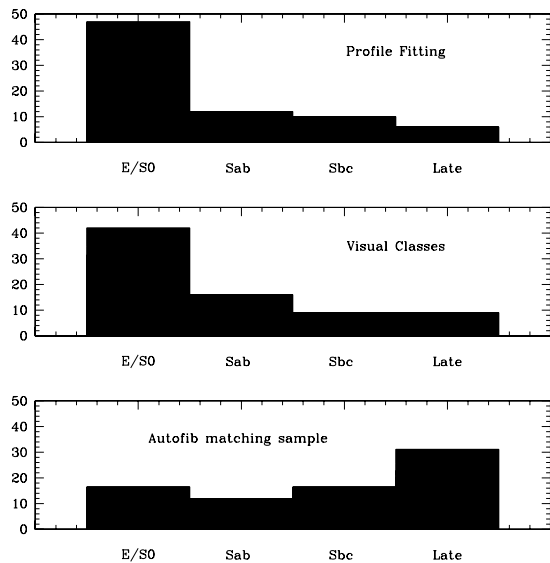


Figure 10 Distribution of host galaxy morphological types. a) EMSS survey: fit parameters, b) EMSS survey: visual inspection c) Autofib survey: randomly-drawn sample (see text).

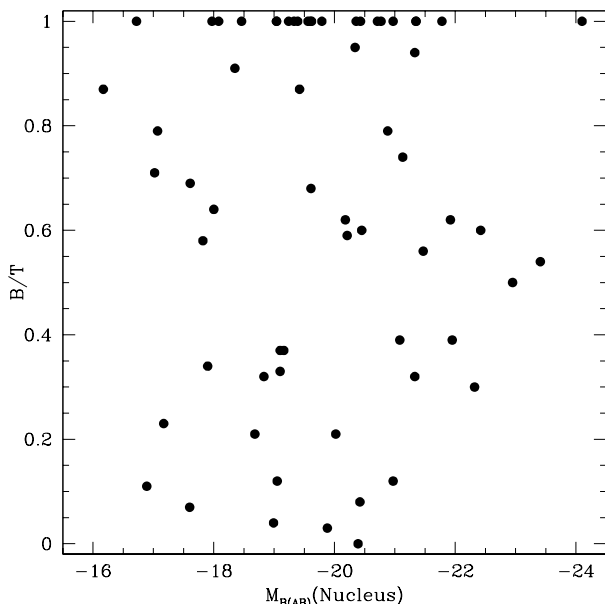


Figure 11 *I* band bulge-to-total luminosity ratio (B/T) plotted as a function of nuclear $M_{B(AB)}$ magnitude.

In Fig. 12 we have plotted the fitted disk and bulge scale lengths against galaxy luminosity. We have also plotted in this diagram the observed size/luminosity relation for ellipticals from Schade, Barrientos, & Lopez-Cruz (1997) and spirals (Freeman 1970). The AGN host galaxies follow these relations surprisingly well, the large scatter caused, in part, by the errors on the parameters in the fitting process.

We can straightforwardly compare the sizes of these host galaxies with those identified with HST by other authors. McLure et al. (1999), Boyce et al. (1997) and Bahcall et al. (1997) all give absolute magnitudes and effective radii

or scale heights for their favoured fit (bulge or disk) to the AGN host galaxies. In the comparison, we have only considered properties of the radio-quiet AGN observed by these authors. To minimise possible discrepancies arising from different fitting procedures, we used the results of the 2D-fitting process employed by all authors. Bahcall et al. (1997) and Boyce et al. (1997) both give host galaxy magnitudes in the *V* passband. To convert this into the $B(AB)$ band we used the following relations:

$$B(AB) = V + 0.78 \quad (\text{bulge})$$

$$B(AB) = V + 0.42 \quad (\text{disk})$$

For McLure et al. (1999), we adopted the following transformations between their *R* passband and the $B(AB)$ band.

$$B(AB) = R + 1.41 \quad (\text{bulge})$$

$$B(AB) = R + 0.99 \quad (\text{disk})$$

Note that the absolute magnitudes derived by these authors correspond to total galaxy luminosity which is fit by a single component i.e. either bulge or disk but not both as in this analysis. Thus the bulge or disk luminosities quoted by these authors will be systematically higher than the similar luminosities derived in this analysis where a bulge plus disk model is fit simultaneously. In general, however, one or other of the components is likely to be dominant (particularly true for bulges) and so the offset will be small.

We have plotted the size-absolute magnitude distribution for these host galaxies alongside those for the EMSS sample in Fig. 12. Although the galaxies are clearly larger and more luminous on average than the EMSS sample, they follow the identical relation to the EMSS AGN and exhibit a large overlap in their properties. From this diagram we conclude that AGN host galaxies exhibit a continuous range of properties, broadly correlated with their nuclear luminosity. To investigate this further, we now consider the detailed correlation between host galaxy and nuclear luminosity.

4.3 Host and Nuclear properties

We have plotted in Fig. 13a) the rest-frame $M_{B(AB)}$ host galaxy absolute magnitude as a function of point source $M_{B(AB)}$. Comparison with Fig. 3 gives an indication of the errors associated with the determination of the host galaxy and nuclear absolute magnitudes at various points in this diagram. There is a weak but significant correlation between the magnitude of the galaxy and the point source AGN component. A Spearman rank test yields a positive correlation at greater than the 3σ level. The least squares fit (slope=0.21) to the points with point source detections (filled circles) is also shown.

In Fig. 13b) we have included the data points from the radio-quiet AGN observed by McLure et al. (1999). In this case the *R* magnitude for the nuclear component was transformed to the *B* band by:

$$B(AB) = R + 0.55$$

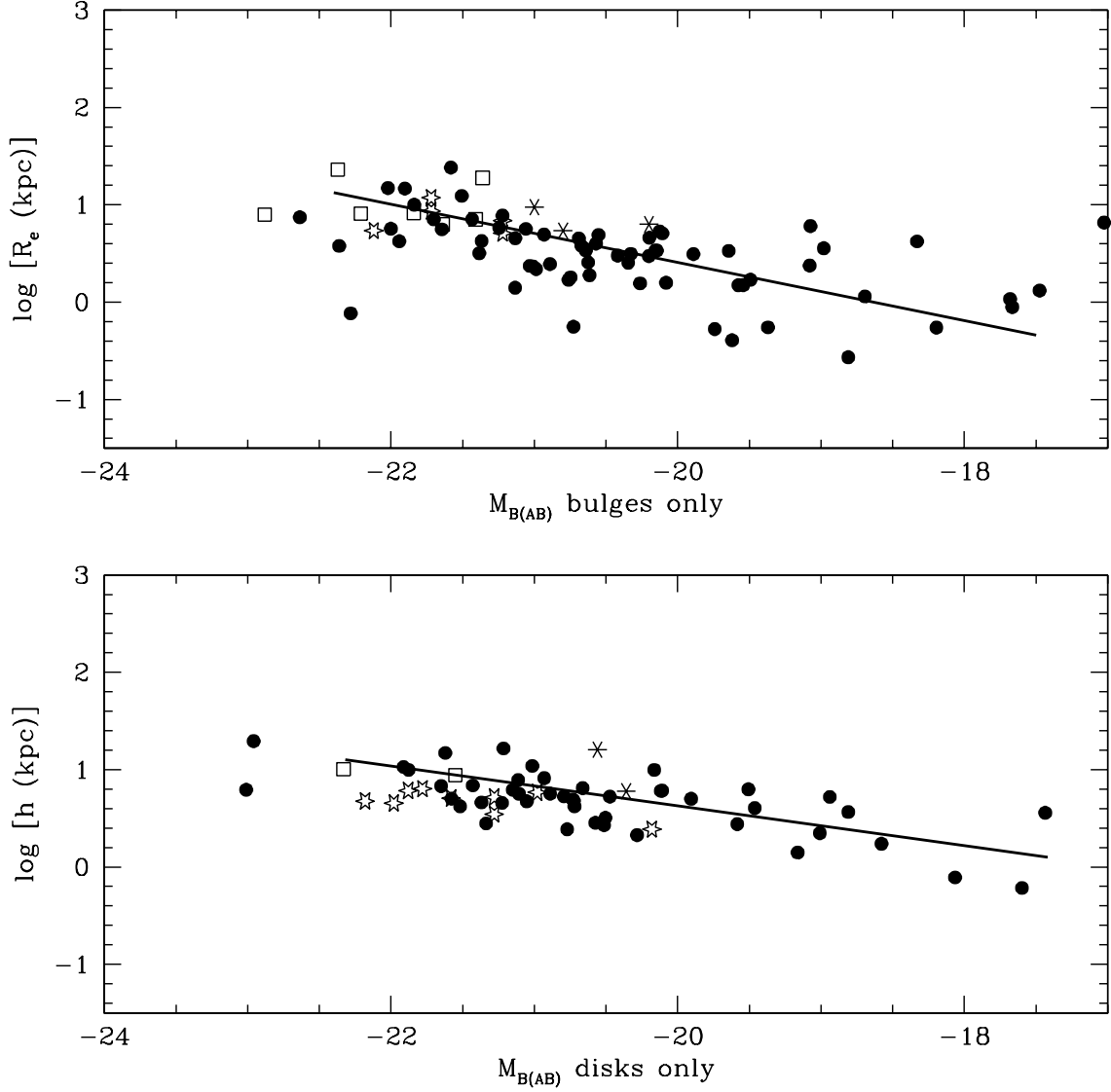


Figure 12 Scale-length $v.$ absolute magnitude for a) bulges b) disks for the host galaxies of the AGN in the sample. The solid lines denote the observed relations for elliptical bulges (Schade, Barrientos, & Lopez-Cruz 1997) and spiral disks (Freeman 1970). Other symbols represent different HST AGN imaging surveys. Open squares: McLure et al. (1999); stars: Bahcall et al. (1997); asterisks: Boyce et al. (1998).

Although at the high luminosity end of the distribution, the data points of McLure et al. (1999) are consistent with the trend seen in the EMSS sample.

We have also added the results of the Bahcall et al. (1997) and Boyce et al. (1997) analysis in Fig 13c). These results are treated separately because the nuclear components in these studies was strongly saturated in the HST images, leading to some uncertainties in the photometry of the point source component. In this case the following relation was used to convert nuclear V band magnitudes into the $B(AB)$ band.

$$B(AB) = V + 0.19$$

Again, these points lie at the high luminosity end of the distribution, although in this case all the points appear systematically shifted toward lower host galaxy luminosities than the trend apparent in this analysis or in the observations of McLure et al. (1999). This could be caused by a strongly saturated nuclear image making it difficult to detect all the galaxy light, or simply the fact that any weak correlation between nuclear and host galaxy luminosity breaks down at the highest luminosities.

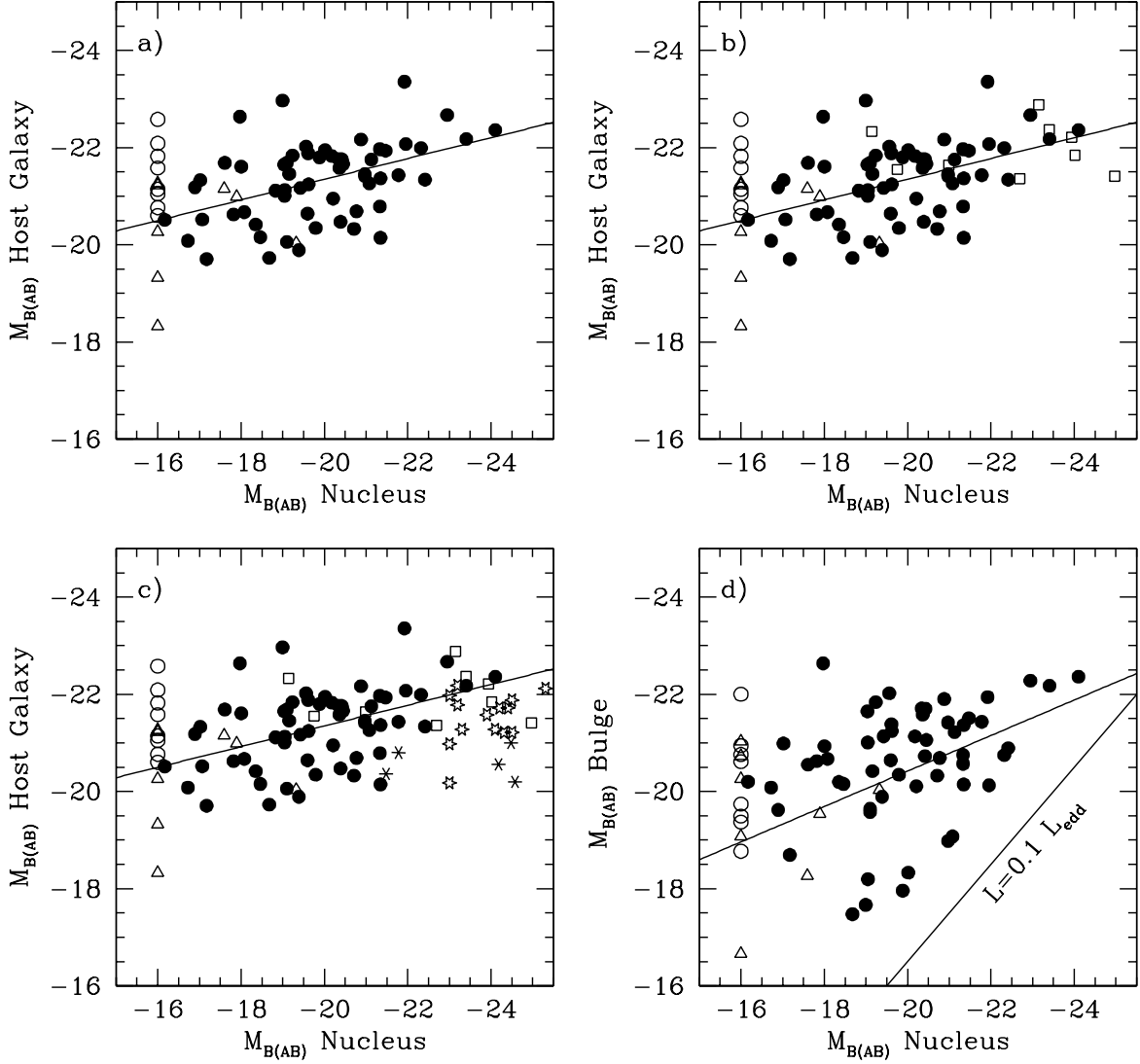


Figure 13 a) Nuclear luminosity v. host galaxy luminosity for all objects imaged in the survey. Open symbols represent those objects with no detectable or weak ($M_{B(AB)} > -16$) point source components. Triangles denote ‘ambiguous’ AGN. b) as figure a) with data-points (open squares) from radio-quiet AGN in the McLure et al. (1999) survey. c) as b) with additional data points from Bahcall et al. (1997) (stars) and Boyce et al. (1998) (asterisks). d) Nuclear luminosity v. bulge luminosity for all objects imaged in the survey. Symbols as for a). Also shown is the predicted relation for AGN with $L = 0.1 L_{\text{Edd}}$ (see text).

However, similar weak correlations have also been found by a number of other authors (e.g. Bahcall et al. 1997, McLeod et al. 1999). This has been potentially ascribed to an underlying correlation between the bulge mass (M_{bulge}) and black hole mass (M_{BH}) where $M_{\text{BH}} = 0.006 M_{\text{bulge}}$ based on the observations of Magorrian et al. (1998). Translating this into a correlation between bulge and nuclear absolute magnitudes, the approximate relation can be obtained (see McLeod et al. 1999):

$$M_{B(AB)\text{AGN}} = M_{B(AB)\text{Bulge}} - 6.0 \\ - 2.5[\log \epsilon + \log(\frac{\Upsilon_{B(AB)}}{10M/L}) + \log(\frac{f}{0.006}) - \log(\frac{BC}{10})]$$

where ϵ is the ratio to Eddington luminosity, $\Upsilon_{B(AB)}$ is the mass-to-light ratio in the $B(AB)$ band, BC is the bolometric correction from $B(AB)$ band luminosity to total luminosity for the AGN, and f is the fraction of the spheroid mass in the black hole. The normalisation constants are the typical observed values for each of these parameters.

Substituting these default values for $\Upsilon_{B(AB)}$, BC and f , the correlation expected for a constant Eddington ratio (in this case $L = 0.1L_{\text{Edd}}$) is shown in Fig. 13d), where we have now plotted bulge luminosity against nuclear luminosity for the EMSS sample. Again we find a correlation which is significant at the 99 per cent confidence level (based on the Spearman rank test) with a least squares slope of 0.36. Based on the black hole model described above, the lower bound of the correlation is consistent with an inferred Eddington ratio of ~ 5 per cent, with most AGN radiating significantly below this limit.

The correlation observed between the host galaxy and nuclear components is, of course, very much flatter than that given by a single Eddington ratio. Such a flat correlation could be explained by appealing to the fact that lower luminosity AGN preferentially radiate at lower Eddington ratios. This would naturally explain the inference that brighter AGN appear to radiate at Eddington ratios up to 20 per cent (McLure et al. 1999, McLeod et al. 1999), see also Fig. 13b) and c).

Perhaps the greatest concern over any correlation is that it may simply be an artifact of the detection limits of our analysis procedure. For example, bright galaxies (in particular bright bulges) might mask the existence of a weak point source. Equally bright point source components might hide faint galaxies (in particular small bulges). Thus the areas of Fig. 13 which might be selected against are precisely those areas in which no data points are seen.

The simulations (section 3.2) that were done to estimate the errors are indicative rather than comprehensive. Nevertheless, they show that relatively faint galaxies can be detected in the presence of a strong point source and that relatively weak point sources can be detected in the presence of bright galaxies (see Fig. 3). These results suggest that the correlation between host galaxy and nuclear luminosity is unlikely to be due to selection effects in the fitting process.

4.4 Interactions

In marked contrast to previous studies of bright AGN (Bahcall et al. 1997, Boyce et al. 1997), few, if any, of the AGN in this study show evidence for interaction or a strong excess of close companions. The latter result is hardly surprising, since Smith et al. (1995) have already demonstrated that the excess number of galaxies around $z < 0.3$ AGN in the EMSS is consistent with clustering strength of field galaxies. Similar results are also reported for Seyfert 1 galaxies (Dultzin-Hacyan et al. 1999).

The frequency of mergers in this sample is harder to put on a quantitative basis. Nevertheless the fit residuals (see Table 2) show little evidence for significant post-merger/interaction activity (e.g. disrupted morphologies, tidal tails etc.). Inner bars and weak spiral structure are the most common residual features seen. As noted by McLure et al. (1999) a definitive measure of the extent to which AGN activity is accompanied by evidence for interactions awaits a detailed study of the level of activity in otherwise ‘normal’ galaxies. A low incidence of tidal tails/multiple nuclei (< 10 per cent) was also noted by Malkan et al. (1998) in their imaging study of lower luminosity Seyfert galaxies.

It is certainly true that the limited depth of our 600-sec HST exposures could lead us to miss low level residuals implying post-merger activity. Nevertheless, the level of strong interactions seen in this low-luminosity AGN sample (< 5 per cent) is much less than has been seen in similar studies of brighter AGN. One possible interpretation is that interactions do not play as strong a role in fuelling lower luminosity AGN ($M_B > -23$). Another explanation might be that lower luminosity AGN represent a more advanced stage of the AGN evolutionary process, i.e. the AGN declines in luminosity with time from the merger event which initially fuelled the AGN.

Unfortunately with the absence of a similarly detailed morphological study of ‘normal’ galaxies it is impossible to determine whether AGN do, in fact, show any strong evidence for any enhanced merger/interaction activity compared to the field galaxy population. From this study, the indication is that there is little, if any, evidence for such activity.

5 CONCLUSIONS

We have carried out a systematic ground- and HST-based imaging study of a large sample of nearby AGN. The X-ray selection of the initial sample minimises any optical morphological bias. Although on average ten times fainter than many previous samples of nearby AGN imaged with HST, the objects studied here comprise the bulk of local AGN, with space densities up to 100 times higher than their more luminous counterparts. As such they are responsible for the vast majority of the AGN luminosity density in the local Universe.

We find that the properties of the host galaxies of these AGN are much more ‘normal’ compared to those of more luminous AGN/QSOs. The host galaxies follow the observed size-luminosity relations for bulges and disks, with sizes typically $10h_{50}$ kpc. The host galaxies span a wide range in luminosity, with a median luminosity of $M_{B(AB)} = -21.5$. All but one of the host galaxies are detected with $M_{B(AB)} > -18$.

Compared to a random sample of field galaxies at these redshifts, the host galaxies are biased towards early morphological types (E, S0). This is consistent with the observation that the host galaxies are also 0.75 ± 0.25 mag brighter than field galaxies at $z < 0.15$. The median luminosity of the sample is also consistent with the most recent estimates of L^* for early spectral types.

There is a weak correlation between the host galaxy and nuclear luminosity, the origin of which may be due to the underlying energy generation mechanism. Assuming the standard black hole model for energy generation in AGN and the derived relation between spheroid and black hole mass, the AGN in this study typically radiate at or below a few per cent of their Eddington luminosity.

There is no evidence for any enhanced merger activity/interactions in this sample of objects. The host galaxies of these AGN thus appear to represent a rather typical subset of ‘normal’ galaxies in the local Universe, albeit biased towards bulge-dominated objects.

When combined with HST imaging studies of brighter AGN, it is clear that the properties of AGN host galaxies

form a continuous distribution, over all sizes and luminosities. The host galaxies of AGN are not unusual with respect to the overall galaxy population. Galaxies with luminosities L^* and fainter are capable of harbouring an AGN. Indeed the correlation which leads the brighter AGN to be found in the large, more luminous galaxies also reveals that the fainter AGN that comprise the bulk of the population in the local Universe will be found in normal galaxies. The underlying parameter driving this correlation may be bulge mass and/or energy generation efficiency.

The HST continues to provide a wealth of information on AGN host galaxies at low redshifts. However, the vast majority of low redshift AGN imaged to date are only of moderate luminosity ($-24 < M_B < -18$). Even the most luminous of low redshift AGN ($M_B \sim -25$) are still significantly fainter than the typical 'break'-luminosity QSOs ($M_B = -26$) at $z \sim 2$, where QSO activity reaches its peak. One of the next major observational steps will therefore be the extension of similarly comprehensive AGN imaging studies to high redshift. It is only by considering unbiased samples over as wide a luminosity as possible that we can hope to disentangle the relationship between the large scale (the host galaxy and its environment) and the small scale (the nucleus and energy generation mechanism) phenomena in AGNs. It is to be hoped that the combination of large aperture and outstanding image quality provided by new ground-based telescopes such as Gemini will yield major advances in this field in the near future.

ACKNOWLEDGEMENTS

The observations were obtained with the Jacobus Kapteyn Telescope at the Observatorio del Roque de los Muchacos operated by the Royal Greenwich Observatory, the 40-inch telescope at Siding Spring operated by the Research School of Astronomy and Astrophysics, Australian National University and with the Hubble Space Telescope operated by STScI. BJB acknowledges the hospitality of Dominion Astrophysical Observatory. We are indebted to Matthew Colless for supplying the Autofib survey galaxy catalogue in digital format. We thank Nicholas Ross and Danielle Frenette for their work on the morphological classifications.

REFERENCES

- Adams T.F., 1977, *ApJS*, 33, 19
 Avni Y., Tanenbaum H., 1986, *ApJ*, 305, 83
 Bahcall J.N., Kirakos, S., Saxe D.H., Schneider D.P., 1997, *ApJ*, 479, 658
 Boyce P.J. et al., 1997, *MNRAS*, 298, 121
 Boyle B.J., McMahon R.G., Wilkes B.J., Elvis M. 1995, *MNRAS*, 276, 315
 Boyle B.J., Shanks T., Peterson B.A., 1988, *MNRAS*, 235, 935
 Dultzin-Hacyan D., Krongold Y., Fuentes-Guridi I., Marziani 1999, *ApJ*, 513, 111
 Dunlop J.S., Taylor G.L., Hughes D.H., Robson E.I., 1993, *MNRAS* 264, 455
 Ellis R.S., Colless M., Broadhurst T., Heyl J., Glazebrook K., 1996, *MNRAS*, 280, 235
 Folkes S. et al., 1999, *MNRAS*, 308, 459
 Freeman K. 1970, *ApJ*, 160, 811
 Kotilainen J., Ward M.J., 1994, *MNRAS*, 266, 953
 Green R., Schmidt M., Liebert J., 1986, *ApJS*, 61, 305
 Landolt 1992, *AJ*, 104, 320
 Maccacaro T., Wolter A., McLean B., Gioia I., Stocke J.T., Della Ceca R., Burg R., Faccini R., 1994, *Ap. Lett. & Comm.*, 29, 267
 Magorrian J. et al., 1998, *AJ*, 115, 2285
 MacKenty J.W., 1990, *ApJS*, 72, 231
 Malkan M.A., Margon B., Chanan G.A., 1984, *ApJ*, 280, 66
 Malkan M.A., Gorjian V., Tam R., 1998, *ApJS*, 117, 25
 McLeod K.K., Reike G.H., 1994, *ApJ*, 431, 137
 McLeod K.K., Reike G.H., Storrie-Lombardi L.J., 1999, *ApJ*, 511, 67
 McLure R.J., Dunlop J.S., Kukula M.J., Baum S.A., O'Dea C.P., Hughes D.H., 1999, *MNRAS*, 308, 377
 Peacock J.A., Miller L., Mead A.R.G., 1986, *MNRAS*, 218, 265
 Piccinotti et al. 1982, *ApJ*, 253, 485
 Sandage A., 1961, *The Hubble Atlas of Galaxies*, (Carnegie Institution: Washington)
 Schade D.J., Barrientos L., Lopez-Cruz O. 1997, *ApJ*, 477, 17
 Schade D.J., Lilly S.J., Le Fèvre O., Hammer F., Crampton D. 1996, *ApJ*, 464, 79
 Simien, de Vaucouleurs G. 1986, *ApJ*, 302, 564
 Simkin S.M., Su H.J., Schwarz M.P., 1980, *ApJ*, 237, 404
 Smith E.P., Heckman T.M., Bothun G.D., Romanshin W., Balick B. 1986, *ApJ*, 306, 64
 Smith E.P., Heckman T.M., 1990, *ApJ*, 348, 38
 Smith R.J., Boyle B.J., Maddox S.J. 1995, *MNRAS*, 277, 270
 Stetson, P., 1987, *PASP*, 99, 191
 Stocke J.T. et al., 1991, *ApJS*, 76, 813
 Taylor G.L., Dunlop J.S., Hughes D.H., Robson E.I., 1996, *MNRAS*, 283, 930
 Terlevich R., Tenorio-Tagle G., Franco J., Melnick J., 1992, *MNRAS*, 255, 713
 Veron-Cetty M.P., Woltjer L., 1990, *A&A*, 236, 69
 Veron-Cetty M.P., Veron P., 1997, *A Catalogue of Active Galactic Nuclei*, 7th Edition
 Zitelli V., Granato G.L., Mandolesi N., Wade R., Danese L., 1993, *ApJS*, 84, 185

This paper has been produced using the Blackwell Scientific Publications \TeX macros.

